Variable-density mixing in buoyancy-driven turbulence

D. LIVESCU AND J. R. RISTORCELLI

Los Alamos National Laboratory, Los Alamos, NM 87544, USA
livescu@lanl.gov

The homogenization of a heterogeneous mixture of two pure fluids with different densities by molecular diffusion and stirring induced by buoyancy-generated motions, as occurs in the Rayleigh–Taylor (RT) instability, is studied using direct numerical simulations. The Schmidt number, Sc, is varied by a factor of 20, $0.1 \leqslant Sc \leqslant 2.0$, and the Atwood number, A, by a factor of 10, $0.05 \leqslant A \leqslant 0.5$. Initial-density intensities are as high as 50% of the mean density. As a consequence of differential accelerations experienced by the two fluids, substantial and important differences between the mixing in a variable-density flow, as compared to the Boussinesq approximation, are observed. In short, *the pure heavy fluid mixes more slowly than the pure light fluid*: an initially symmetric double delta density probability density function (PDF) is rapidly skewed and, only at long times and low density fluctuations, does it relax to a Gaussian-like PDF. The heavy–light fluid mixing process asymmetry is relevant to the nature of molecular mixing on different sides of a high-Atwood-number RT layer. Diverse mix metrics are used to examine the homogenization of the two fluids. The conventional mix parameter, θ, is mathematically related to the variance of the excess reactant of a hypothetical fast chemical reaction. Bounds relating θ and the normalized product, $\varXi$, are derived. It is shown that θ underpredicts the mixing, as compared to $\varXi$, in the central regions of an RT layer; in the edge regions, θ is larger than $\varXi$. The shape of the density PDF cannot be inferred from the usual mix metrics popular in applications. For example, when θ, $\varXi \geqslant 0.6$, characteristic of the interior of a fully developed RT layer, the PDFs can have vastly different shapes. Bounds on the fluid composition using two low-order moments of the density PDF are derived. The bounds can be used as realizability conditions for low-dimensional models. For the measures studied, the tightest bounds are obtained using $\varXi$ and mean density. The structure of the flow is also examined. It is found that, at early times, the buoyancy production term in the spectral kinetic energy equation is important at all wavenumbers and leads to anisotropy at all scales of motion. At later times, the anisotropy is confined to the largest and smallest scales: *the intermediate scales are more isotropic than the small scales*. In the viscous range, there is a cancellation between the viscous and nonlinear effects, and the buoyancy production leads to a persistent small-scale anisotropy.

1. Introduction

Molecular mixing in response to stirring by turbulence is an important process in many practical applications. If the microscopic densities of the fluids participating in the mixing are very different we refer to such flows as variable-density (VD)

flows in contrast to the Boussinesq approximation in which the densities are commensurate. In a VD flow the velocity field is no longer solenoidal and the specific volume, a function of the amount of each material present, is a dependent variable. VD mixing is encountered in atmospheric and ocean flows, astrophysical flows, combustion and many flows of chemical engineering interest (Givi 1989). Many of these flows are driven by acceleration (e.g. gravity in geophysical and astrophysical flows) which, because of the large density differences, leads to large differential fluid accelerations.

Here, a simple form of multi material mixing between two miscible fluids with different microscopic densities (Besnard *et al.* 1992, Livescu & Ristorcelli 2007), driven by a constant external acceleration, as occurs in the Rayleigh–Taylor (RT) instability, is studied.

The paper is motivated by the need to understand the new physics associated with mixing in the presence of differential acceleration effects. It is also motivated by the very limited data that exist for the derivation and testing of closures for VD RT transition and turbulence. The properties of the turbulence and mixing in such VD flows, when they have been studied, are typically obscured by the presence of inhomogeneities due to edge effects and walls. The current investigation focuses on the nonlinear dynamics and statistics of buoyantly driven turbulence in the statistically homogeneous problem. The physical situation we study is similar to the buoyantly generated turbulence in the Boussinesq approximation studied by Batchelor, Canuto & Chasnov (1992). Here, the high-Atwood-number VD problem is treated. As such, the new nonlinearities due to very large density variations in the advective terms of the Navier–Stokes equations are important. The statistical form of the equations for this problem, except for the inhomogeneous flux terms, also describes the RT mixing layer. Thus, the current homogeneous simulations include the same buoyancy generation and the same nonlinear cascade mechanisms as occur in the RT layer. The present configuration is also more computationally effective than the RT case: the statistical variability of the volumetric ensembles, as opposed to RT in which the ensemble is planar, are substantially reduced. The inhomogeneous RT transport terms, that do not occur in this configuration, are important at the edges of the layer. In principle, the current homogeneous simulations describe the core of a fully developed (wide) RT layer after a time at which enough mixing occurs such that little pure fluid reaches the centreline. This time can be inferred by inspection of the centreline density kurtosis given by Ristorcelli & Clark (2004).

The current VD problem was first addressed in Sandoval (1995) and Sandoval, Clark & Riley (1996); their study focused on the hydrodynamics statistics of the flow. Our interest is: (i) in the statistics of the active scalar field; (ii) useful measures of the state and rate of the material mixing; and (iii) changes in the structure of the flow induced by the differential accelerations. Metrics related to the hydrodynamics have been discussed in the earlier companion paper, Livescu & Ristorelli (2007, hereinafter referred to as LR). Summaries of RT simulation studies can be found in the overviews of Dalziel, Linden & Youngs (1999) and Young *et al.* (1999) and references therein. Additional commentary may be found in Ristorcelli & Clark (2004). Throughout this study, several observations and analogies with the RT problem are made; all such extensions presented here have been verified with the 3072^3 RT data of Cabot & Cook (2006) as shown in Livescu *et al.* (2008). Nevertheless, the results presented are more general and have application to other VD flows.

1.1. *The variable-density-flow model*

This paper treats active mixing in low-speed flows in which the turbulent Mach number is small and the fluids participating in the mixing are incompressible. In this case, the macroscopic specific volume is related to the mass fractions of the two fluids by

$$v = \frac{1}{\rho} = \frac{Y_1}{\rho_1} + \frac{Y_2}{\rho_2}, \tag{1.1}$$

where $Y_1 + Y_2 = 1$. Here, ρ_1 and ρ_2 are the constant 'microscopic densities' of the pure fluids, i.e. $\rho_1 = m_1/V_1$ and $\rho_2 = m_2/V_2$. The subscript '2' refers to the heavier fluid.

For compressible ideal gasses, the density can be expressed using the equation of state:

$$\rho = \frac{P}{\mathscr{R}T(Y_1/W_1 + Y_2/W_2)}. \tag{1.2}$$

where W_i, $i = 1, 2$, are the molar masses of the two fluids and $\mathscr{R}$ is the universal gas constant. The current approximation corresponds to the case where P/T is approximately constant. The equation of state, (1.2), leads to (1.1) when $\rho_i = W_i P/\mathscr{R}T$.

The primary non-dimensional parameter characterizing the differential acceleration effects is the Atwood number:

$$A = \frac{\rho_2 - \rho_1}{\rho_2 + \rho_1} \quad \Rightarrow \quad \frac{\rho_2}{\rho_1} = \frac{1 + A}{1 - A}. \tag{1.3}$$

For air interpenetrating helium, $A = 0.75$; for air and hydrogen, $A = 0.85$. Similar Atwood numbers occur for mixing between liquid hydrocarbons and air. In the current VD simulations the largest density intensities are $i_\rho = \rho_{rms}/\bar{\rho} \sim 0.5$ at initialization. In the Boussinesq limit, $i_\rho \sim 0$; for select combustion flows, $i_\rho \sim 2$.

The current flow can be understood as a pressure-gradient-driven flow in which the differential accelerations of the two fluids are important. In this VD flow, it is the very large mean pressure gradient due to buoyancy that, coupled with the mass flux, creates turbulence and drives the material mixing (LR). Such fluid physics occurs, more generally, in any acceleration-driven flow involving different-density fluids.

1.2. *Highlights of this study*

In this paper, new mixing physics that might result from large differential fluid accelerations, as occurs in pressure-gradient-driven VD flows, is investigated. Our study makes contributions in the following areas.

(i) A detailed comparison of active scalar mixing in a VD flow is contrasted to mixing in the Boussinesq (small density differences) case.

(ii) Comparison of mix metrics and their use in describing mixing in the VD case.

(iii) The effects of buoyancy on the energy spectrum and small-scale universality.

(iv) The generation of an archival database to develop closures for VD turbulence.

The first portion of the paper, §2, provides the problem statement summarizing the equations and the initial conditions. Section 3 details our study of the mix state using different conventional mix metrics. Section 4 studies the mixing rate. Section 5 studies the small-scale motions and spectral structure of the buoyantly driven mixing. Section 6 gives a summary of findings and 7 the conclusions. For the numerical method see LR.

2. Governing equations and simulation cases

The equations describing the mixing between two miscible fluids with different microscopic densities, ρ_1 and ρ_2, are the Navier–Stokes equations and species mass fraction transport equations. After non-dimensionalizing with $\rho_0 = 0.5(\rho_1 + \rho_2)$ and reference velocity and length scales, U_0 and L_0, the equations can be written as (see LR):

$$\rho^*_{,t} + (\rho^* u^*_j)_{,j} = 0, \tag{2.1}$$

$$(\rho^* u^*_i)_{,t} + (\rho^* u^*_i u^*_j)_{,j} = -p^*_{,i} + \tau^*_{ij,j} + \frac{1}{Fr^2}\rho^* g_i, \tag{2.2}$$

$$u^*_{j,j} = -\frac{1}{Re_0 Sc}(\ln \rho^*)_{,jj}, \tag{2.3}$$

with $\tau^*_{ij} = (u^*_{i,j} + u^*_{j,i} - 2/3 u^*_{k,k}\delta_{ij})/Re_0$. The primary dependent variables are the density ρ^*, velocity in the x_i-direction u^*_i, and pressure p^*. The superscript $*$ is used to denote total instantaneous (mean plus fluctuation) values. The non-dimensional parameters in (2.1)–(2.3) are the computational Reynolds number, Re_0, Schmidt number, Sc, and Froude number, Fr:

$$Re_0 = \rho_0 L_0 U_0/\mu_0, \qquad Sc = \mu_0/\rho_0 D_0, \qquad Fr^2 = U_0^2/gL_0, \tag{2.4}$$

with g, the magnitude of the acceleration due to gravity, taken to be constant. The dynamic viscosity, μ_0, and diffusion coefficient, D_0, are constant and μ_0 is the same for both fluids. In the equations above, the non-dimensional instantaneous density varies between $1 - A(t)$ and $1 + A(t)$ where $A(t)$ is the instantaneous Atwood number.

In the subsequent sections, capital italic letters, overbars and angle brackets are used to denote mean values. Angle brackets are preferred for longer expressions while overbars are used for quantities named with greek letters. Lower-case letters (italic or greek) or primes are used to denote fluctuations. As the density is not spatially uniform, some of the results are presented using density-weighted (Favre) averages, denoted with a tilde, and the corresponding fluctuations with double primes. Thus, the instantaneous velocity, density, pressure and specific volume are decomposed as $u^*_i = U_i + u_i = \tilde{U}_i + u''_i$, $\rho^* = \bar{\rho} + \rho$, $p^* = P + p$ and $v^* = V + v$, respectively. Note that $\tilde{U}_i - U_i = u_i - u''_i = a_i$. The definitions for the normalized mass flux, a_i, Favre Reynolds stresses, R_{ij}, and turbulent kinetic energy, $\tilde{k}$, and total kinetic energy, E_K, are given below:

$$a_i = \frac{\langle u_i \rho \rangle}{\bar{\rho}} = -\langle u''_i \rangle, \tag{2.5}$$

$$R_{ij} = \langle \rho^* u''_i u''_j \rangle = \bar{\rho}\langle u_i u_j \rangle - \bar{\rho}a_i a_j + \langle \rho u_j u_j \rangle, \qquad R_{kk} = 2\bar{\rho}\tilde{k}, \tag{2.6}$$

$$E_K = \langle \rho^* u^*_i u^*_i \rangle/2. \tag{2.7}$$

2.1. *Solution method and initial conditions*

Equations (2.1)–(2.3) are those governing the flow generated by the VD RT instability (e.g. see Sandoval 1995; Cook & Dimotakis 2001). In this study, the equations are solved in a triply periodic domain, corresponding to a statistically homogeneous flow, and the averages are calculated as volume averages. Such a configuration eliminates the complications due to the presence of non-periodic boundaries while allowing fundamental turbulence studies in the presence of buoyancy and VD effects in the context of mixing between initially segregated materials. In addition, more data are available for statistics calculations in the present configuration than for an

inhomogeneous problem, greatly reducing the statistical variability. In physics, the flow corresponds to the inner region of a fully developed Rayleigh–Taylor mixing layer. In modelling, this is a benchmark problem which any turbulence model for the VD RT should handily predict. In flow physics, this benchmark problem allows the study of the peculiar nature of the mixing between two different-density fluids and, thus, the results presented are more general than the RT problem.

The density field is initialized as random blobs of pure fluids, corresponding to a double-delta PDF. The velocity field is initialized with a zero solenoidal part and dilatational part given by:

$$u_i = -\frac{1}{Re_0 Sc}(\ln \rho^*)_{,i}, \tag{2.8}$$

which satisfies (2.3).

Equations (2.1)–(2.3) are solved using a pseudospectral algorithm. The equations are integrated in time using a second-order Adams–Bashforth method in conjunction with a pressure projection method which integrates the momentum equations in two steps: first without the pressure terms and then adding these terms to restore the correct divergence of velocity. The aliasing errors introduced by calculating the nonlinear terms in real space are partially controlled using truncation and ensuring that the amount of energy in the wavenumbers affected by aliasing is small. More details about the numerical approach, including improvements over standard methods, are given in LR.

A few comments regarding the mean pressure gradient in VD flows are now given. In VD turbulence with arbitrary boundary conditions, the two first-order moments, the mean pressure gradient, P_i, and the mean specific volume, V, are dynamical variables evolving as the mixing proceeds. For the present triply periodic simulations:

$$P_{,i} = \frac{\bar{\rho}}{1 - \langle \rho v \rangle}(g_i + \langle u_i u_{j,j} \rangle - \langle v p_{,i} \rangle + \langle v \tau_{ij,j} \rangle) \qquad U_{i,t} = 0, \tag{2.9}$$

$$\bar{\rho} V = 1 - \langle \rho v \rangle. \tag{2.10}$$

In the Boussinesq case, both $P_{,i} = \bar{\rho} g_i$ and V are constant. For periodic boundary conditions, the VD mean pressure can be determined only to a constant gradient, which is a free parameter. This is chosen, as given by (2.9) such that the energy conversion of potential to kinetic energy is maximized (see LR). Note that the addition of a spatially constant mean pressure gradient to the equations does not change their translational invariance and the fluctuations remain periodic.

2.2. Simulation cases

Table 1 provides relevant information for the cases studied. For all cases, $\mathbf{g} = (0, 0, -1)$. There are two Reynolds numbers, Re_0 and a static buoyancy Reynolds number, Re_{0b}. Re_0 is a non-dimensional viscosity as it is changed by changing μ_0. Re_{0b} is formed from an effective velocity related to the buoyancy forces and the initial integral scale of the density field. The static buoyancy Reynolds number expresses the ratio of buoyancy and viscous forces at the time g is first applied. The velocity is calculated based on the potential energy corresponding to a height equal to the density integral scale. The dimensional potential velocity is $\sqrt{L_{0_\rho} A g}$, with L_{0_ρ} the dimensional initial density integral scale, so that

$$Re_{b_0} = \frac{\rho_0 \sqrt{L_{0_\rho}^3 A g}}{\mu_0} = Re_0 \sqrt{L_\rho^3 A / Fr^2}, \tag{2.11}$$

Case number	A	$1/Fr^2$	Sc	Re_0	Re_{b_0}	$\langle\rho^2\rangle/\overline{\rho}^2\vert_{t=0}$	$\langle\rho v\rangle\vert_{t=0}$	Resolution
1Base	0.05	1.0	1.0	250	11	0.0024	−0.0024	256^3
1Fr	0.05	10.0	1.0	250	35	0.0024	−0.0024	256^3
1Re1	0.05	1.0	1.0	833	37	0.0024	−0.0024	256^3
1Re2	0.05	1.0	1.0	1667	73	0.0024	−0.0024	512^3
2Sc0	0.25	1.0	0.1	250	26	0.057	−0.061	256^3
2Sc1	0.25	1.0	0.5	250	26	0.057	−0.061	256^3
2Base	0.25	1.0	1.0	250	26	0.057	−0.061	256^3
2Sc2	0.25	1.0	2.0	250	26	0.057	−0.061	256^3
2Re1	0.25	1.0	1.0	833	87	0.06	−0.064	512^3
2Re2	0.25	1.0	1.0	1667	174	0.061	−0.0066	1024^3
3Sc1	0.5	1.0	0.5	250	37	0.22	−0.29	256^3
3Base	0.5	1.0	1.0	250	37	0.22	−0.29	256^3
3Sc2	0.5	1.0	2.0	250	37	0.22	−0.29	512^3

TABLE 1. parameters for the DNS cases.

where $L_\rho = L_{0_\rho}/L_0$. In general, the higher Re_{b0}, the larger the maximum kinetic energy of the flow generated.

The cases described in table 1 were chosen to investigate the influence of the Atwood, Reynolds, Schmidt and Froude numbers. There are three base cases (1Base, 2Base, 3Base) corresponding to the Atwood numbers 0.05 (Boussinesq limit), 0.25 and 0.5. The rest of the cases have one value of the parameters Sc, Re and Froude numbers changed, compared to the base cases. Cases with the same last number in the name have the same value of the respective changed parameter (i.e. both cases 1Re1 and 2Re1 have $Re_0 = 833$). In addition, the Froude number was changed for case 1Fr to match A/Fr^2 from case 3Base. Thus, cases 1Re1, 1Fr and 3Base have about the same Re_{b_0}, but different Re_0, A or Fr. To reduce statistical variability, each simulation is repeated several times with initial conditions generated using different random number seeds. All data presented represent averages over 5 to 10 realizations. The high-Reynolds-number cases 1Re2 and 2Re2 were performed only up to the time when the kinetic energy peaks, $t/t_r \approx 2.5$, where $t_r = \sqrt{Fr^2/A}$ (see LR).

3. VD mixing: assessing the mixing state

A comprehensive study of various mix metrics, in the context of the density PDF and the question of 'how much pure and mixed fluids is present' is now undertaken. To simplify the presentation, the pure heavy, pure light and mixed fluids are called black, white and grey, respectively. The grey fluid can be either (i) 'fully mixed' if the two fluids are completely mixed in equal proportion so that the density is $(\rho_1 + \rho_2)/2$ or (ii) 'partially mixed' otherwise.

3.1. *The θ mix metric*

The quantity $\theta = 1 - \langle\rho^2\rangle/\langle\rho^2\rangle_{nm}$, is commonly used as a mixing-state metric (Youngs 1991; Linden, Redondo & Youngs 1994; Dalziel *et al.* 1999; Ristorcelli & Clark 2004). Youngs (1991) and Linden *et al.* (1994) use

$$\theta = \frac{\langle f_1 f_2\rangle}{\langle f_1\rangle\langle f_2\rangle} \tag{3.1}$$
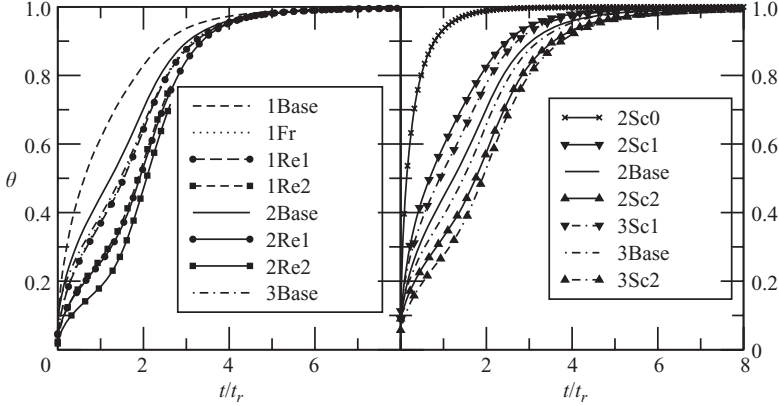
FIGURE 1. Mixing progress as indicated by the evolution of the normalized density variance.

as the mix progress variable, where $f_1 = (\rho - \rho_1)/(\rho_2 - \rho_1)$ and $f_2 = (\rho_2 - \rho)/(\rho_2 - \rho_1)$, so that

$$\theta = 1 - \frac{\langle \rho^2 \rangle}{(\bar{\rho} - \rho_1)(\rho_2 - \bar{\rho})} = 1 - \frac{\langle \rho^2 \rangle}{\langle \rho^2 \rangle_{nm}}. \tag{3.2}$$

The subscript nm refers to the no-mix value of the quantity in question; $\langle \rho^2 \rangle_{nm} = (\rho_2 - \bar{\rho})(\bar{\rho} - \rho_1)$. For the present flow, the no-mix value is $\langle \rho^2 \rangle_{nm} \approx \langle \rho^2 \rangle|_{t=0}$. Figure 1 shows the evolution of θ for the cases considered. In scaled time, mixing is slower for cases with larger Re_{b_0} or higher Sc numbers, even though the kinetic energy is higher. Note that the A, Re_0 and Fr influences can be collapsed using the one parameter, Re_{b_0}, as figure 1 indicates. Note also that as Re_{b_0} is increased, the relative change in θ is smaller (compare cases 1Base, 1Re1 and 1Re2 or cases 2Base, 2Re1 and 2Re2) suggesting a weakening dependence on the Reynolds number at higher Reynolds numbers. This is consistent with the fully developed VD RT results obtained by Cabot & Cook (2006).

3.2. *Mixing state described using the fast reaction analogy*

The scalar field is composed of regions of pure fluids and mixed fluid: white, black or grey. One way to differentiate among the mixed regions is to consider a hypothetical fast reaction and measure the amount of product, which is to say the amount of fully mixed fluid (Cook & Dimotakis 2001). Thus, fully mixed fluid contains a stoichiometric mixture of the two fluids. Any grey region is then composed of product (fully mixed fluid) and excess reactant; the excess reactant may be either one of the two pure fluids, but not both. If the excess reactant is not zero (i.e. the region is not completely homogenized at the stoichiometric proportion) we call the region partially mixed. If a reaction of the type $\nu_1 W + \nu_2 B \rightarrow (\nu_1 + \nu_2)P$, with W (white) the light fluid and B (black) the heavy fluid, is considered, the product mole fraction is defined by:

$$X_P = \begin{cases} \dfrac{\nu_1 + \nu_2}{\nu_2} \dfrac{\rho^* - \rho_1}{\rho_2 - \rho_1} & \text{for} \quad \rho^* \leqslant \dfrac{\nu_1 \rho_1 + \nu_2 \rho_2}{\nu_1 + \nu_2}, \\[3mm] \dfrac{\nu_1 + \nu_2}{\nu_1} \dfrac{\rho_2 - \rho^*}{\rho_2 - \rho_1} & \text{for} \quad \rho^* \geqslant \dfrac{\nu_1 \rho_1 + \nu_2 \rho_2}{\nu_1 + \nu_2}. \end{cases} \tag{3.3}$$

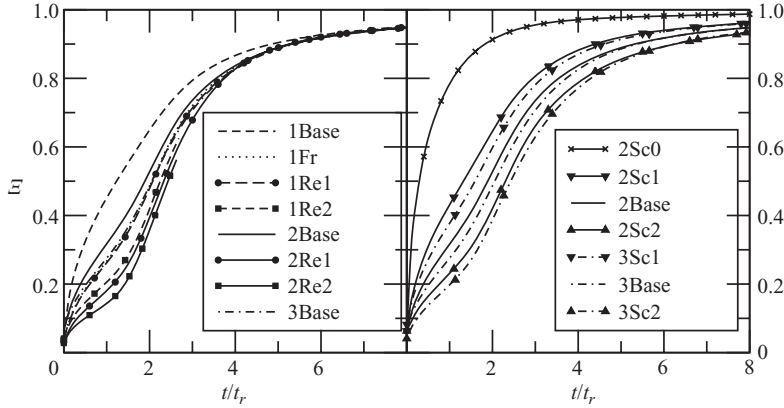FIGURE 2. Mixing progress as indicated by the evolution of the normalized averaged product mole fraction $\varXi$.

Thus, $\langle X_P \rangle$ represent the average product in the domain or, equivalently, the mole fraction of the fluid at the fully mixed mean density. We consider $\langle X_P \rangle$ to be one of the more useful lower-order metrics describing the mix state.

The formulae above were derived using the binary mixture relations $X_1 = (\rho^*/\rho_1)Y_1 = (\rho_2 - \rho^*)/(\rho_2 - \rho_1)$ and $X_2 = (\rho^*/\rho_2)Y_2 = (\rho^* - \rho_1)/(\rho_2 - \rho_1)$ (see e.g. Williams 1985). Maximum product is obtained as $X_{P_{\max}} = X_P(\rho^* = \bar{\rho})$. For the present case, assuming $\nu_1 = \nu_2 = 1$ and $X_{P_{\max}} = 1$.

In the classical RT configuration, the averages are horizontal area averages, and $\langle X_P \rangle$ varies with height. A useful state metric that allows comparison at different heights is defined as (Cook & Dimotakis 2001; Cook & Zhou 2002):

$$\varXi = \frac{\langle X_P \rangle}{X_{P_{\max}}}. \tag{3.4}$$

Figure 2 shows the evolution of $\varXi$, or equivalently $\langle X_P \rangle$ for the current homogeneous RT. At early times, $\varXi$ depends on both Re_{b_0} and Sc numbers. The $\varXi$ variation shows that, in scaled time, mixing is slower for cases with higher Re_{b_0} or Sc numbers. As is the case with θ, the influences of A, Re_0 and Fr are collapsed using only the intial Re_{b_0}. The results confirm that at higher Re_{b_0}, the change in initial buoyant Reynolds number has an ever smaller influence on the mixing progress, again suggestive of the fully developed RT results of Cabot & Cook (2006). At late times, $\varXi$ becomes independent of Re_{b_0}, and only Sc plays a role in the asymptotic evolution.

3.3. *Relations between θ, $\langle X_P \rangle$ and $\varXi$*

Analytic connections can be made between θ, $\langle X_P \rangle$ and $\varXi$. The excess reactant (either white or black) mole fraction is $X_e = 1 - X_P$. In the regions where the light fluid is in excess of the stoichiometric value, $\nu_2 X_1 - \nu_1 X_2 \geqslant 0$ and $X_e = X_1 - (\nu_1/\nu_2)X_2$. In the regions where heavy fluid is in excess of the stoichiometric value, $\nu_2 X_1 - \nu_1 X_2 \leqslant 0$ and $X_e = X_2 - (\nu_2/\nu_1)X_1$. The excess reactant mole fraction is then:

$$X_e = \begin{cases} \dfrac{\nu_1\rho_1 + \nu_2\rho_2 - \rho^*(\nu_1 + \nu_2)}{\nu_2(\rho_2 - \rho_1)} & \text{for} \quad \rho^* \leqslant \dfrac{\nu_1\rho_1 + \nu_2\rho_2}{\nu_1 + \nu_2}, \\[4mm] -\dfrac{\nu_1\rho_1 + \nu_2\rho_2 - \rho^*(\nu_1 + \nu_2)}{\nu_1(\rho_2 - \rho_1)} & \text{for} \quad \rho^* \geqslant \dfrac{\nu_1\rho_1 + \nu_2\rho_2}{\nu_1 + \nu_2}. \end{cases} \tag{3.5}$$

For example, if there are 100 molecules in a control volume and 40 of them are white and 60 black then, if $v_1 = v_2 = 1$, $X_P = 0.8$ and $X_e = 0.2$ and the formula above reduces to:

$$X_e = \left| \frac{\rho_1 + \rho_2 - 2\rho^*}{\rho_2 - \rho_1} \right|. \tag{3.6}$$

The excess reactant and its variance are then written as:

$$X_e = \left| \frac{\tilde{\rho} - \rho}{\rho_2 - \bar{\rho} - \tilde{\rho}} \right| = \left| \frac{\tilde{\rho} - \rho}{\bar{\rho} - \rho_1 + \tilde{\rho}} \right|, \tag{3.7}$$

$$\langle X_e^2 \rangle = \frac{\langle \rho^2 \rangle + \tilde{\rho}^2}{\langle \rho^2 \rangle_{nm} + \tilde{\rho}^2}, \tag{3.8}$$

given only the variance of density and its mean, we can predict the variance of the excess reactant. Here, $\tilde{\rho} = (\rho_2 + \rho_1)/2 - \bar{\rho}$ is the difference between the average density and the average density if the two fluids are present in equal amounts. In the RT layer, $\tilde{\rho}$ depends on height. On re-arranging, we obtain an expression for θ:

$$\theta = \left(1 - \langle X_e^2 \rangle \right) \left(1 + \frac{\tilde{\rho}^2}{\langle \rho^2 \rangle_{nm}} \right). \tag{3.9}$$

Given $\bar{\rho}$, there is a one to one correspondence between the conventional measure θ and $\langle X_e^2 \rangle$. Using $X_e = 1 - X_P$ and the definition of $X_{P_{\max}}$, θ can be written as:

$$\theta = \frac{1 - \langle X_e^2 \rangle}{X_{P_{\max}} (2 - X_{P_{\max}})} = \frac{2\langle X_P \rangle - \langle X_P^2 \rangle}{2\langle X_{P_{\max}} \rangle - X_{P_{\max}}^2} = \varXi \, \frac{2 - \langle X_P^2 \rangle / \langle X_P \rangle}{2 - X_{P_{\max}}}. \tag{3.10}$$

For the present simulations, $\tilde{\rho} = 0$ and $\langle X_e^2 \rangle$ and θ become:

$$\langle X_e^2 \rangle = \frac{\langle \rho^2 \rangle}{(\rho_2 - \bar{\rho})(\bar{\rho} - \rho_1)}, \tag{3.11}$$

$$\theta = 1 - \langle X_e^2 \rangle = \varXi \left(2 - \frac{\langle X_P^2 \rangle}{\langle X_P \rangle} \right). \tag{3.12}$$

For the non-dimensionalization used here $(\rho_2 + \rho_1)/2 = 1$, but for the sake of generality this equality is not used in the derivations.

3.4. *Differences between θ, $\langle X_P \rangle$ and $\varXi$ in the RT layer*

The differences between θ, $\langle X_P \rangle$ and $\varXi$ in the RT mixing layer are now discussed. In the asymptotic VD RT layer, $\varXi_\infty$ varies between 0.6 and 1.0 (Livescu *et al.* 2008). The normalized integral of $\varXi$ across the layer is about 0.8 (Cabot & Cook 2006). In the fully developed experimental RT layer for the Boussinesq case, a number of values are reported: Ramaprabhu & Andrews (2004) give $\theta_\infty = 0.7$ and from Muenshke, Andrews & Schilling (2006) $\theta_\infty = 0.6$. For the Boussinesq simulations of Ristorcelli & Clark (2004) and Dalziel *et al.* (1999), $\theta_\infty = 0.8$. At earlier times, slowly varying smaller values are seen in simulations and experiments, $\theta \approx 0.5 - 0.7$. Bounds relating $\theta, \langle X_P \rangle$ and $\varXi$ are now derived.

Centre of the RT layer

If $\bar{\rho} \approx (\rho_1 + \rho_2)/2$, which is true near the RT layer centreline and for the present simulations, then $X_{P_{\max}} \approx 1$. In this case, since $\langle X_P^2 \rangle / \langle X_P \rangle \leqslant 1$, we find that $\theta \geqslant \varXi \approx \langle X_P \rangle$. The equality corresponds to fully mixed or fully segregated fluids. Thus,

in regions with approximately equal amounts of the two fluids, θ always overpredicts the amount of mixing compared to Ξ, or $\langle X_P \rangle$ (see also figure 3).

Rigorous analytical bounds can also be derived for the difference between these measures when $X_{P_{max}} \approx 1$. As in this case $\Xi \approx \langle X_P \rangle$, all the relations derived below are the same in terms of $\langle X_P \rangle$. From (3.10), we obtain:

$$\theta = 2\Xi - \Xi^2 - \langle X_P'^2 \rangle. \tag{3.13}$$

The minimum value for $\langle X_P'^2 \rangle$ is zero and is obtained when the product (fluid in stoichiometric proportion) is uniformly distributed. Note that $X_P = \langle X_P \rangle + X_P'$. The maximum value of X_P is $\langle X_P \rangle (1 - \langle X_P \rangle)$ and corresponds to the fluid composed only of fully mixed and pure fluid (white or black). In this case, $\langle X_P^2 \rangle = \langle X_P \rangle$, as X_P is either 1 or 0. Thus, for $X_{P_{max}} \approx 1$, we obtain two inequalities for θ:

$$2\Xi - \Xi^2 \geqslant \theta \geqslant \Xi. \tag{3.14}$$

For example, if $\Xi = 0.8$ then $0.8 \leqslant \theta \leqslant 0.96$ with any value in the interval being possible. If $\Xi = 0.6$ then $0.6 \leqslant \theta \leqslant 0.84$. Conversely, the first inequality can be rewritten for Ξ, after examining the roots of the associated second-order polynomial:

$$\theta \geqslant \Xi \geqslant 1 - \sqrt{1 - \theta}. \tag{3.15}$$

For $\theta = 0.8, 0.6$, seen in different RT experiments, $\Xi \geqslant 0.55, 0.36$. We note that for the present simulations, $\Xi \approx 0.62$ corresponds to $\theta = 0.8$ with slight differences among the cases.

Edges of the RT layer

At the edges of the RT layer, $\rho^* \leqslant (\rho_1 + \rho_2)/2$ everywhere or $\rho^* \geqslant (\rho_1 + \rho_2)/2$ everywhere, $\langle X_P \rangle = X_{P_{max}}$, $\Xi = 1$ and $\theta \leqslant 1$ (the equality corresponds to pure fluid). In these regions, θ always underpredicts the amount of mixing compared to Ξ. The lower bound for θ is obtained when the region consists of fully mixed or pure fluid points only, so that $\langle X_P^2 \rangle = \langle X_P \rangle$. Thus,

$$1 \geqslant \theta \geqslant \frac{1}{2 - X_P} = \begin{cases} \dfrac{\rho_2 - \rho_1}{2(\rho_2 - \bar{\rho})} & \text{at the spike side,} \\ \dfrac{\rho_2 - \rho_1}{2(\bar{\rho} - \rho_1)} & \text{at the bubble side.} \end{cases} \tag{3.16}$$

As $\langle X_P \rangle \to 0$, the right bound becomes 0.5. However, this value is never reached, as $\theta = 1$ when $\langle X_P \rangle = 0$.

Ξ underpredicts, in general, the extent of the mixing layer, since $\Xi = 1$ near the edges of the RT layer and there can be significant amount of grey fluid in these regions. As a consequence, Ξ is not used to calculate the width of the RT layer; e.g. Cook & Dimotakis (2001) define the extent of the mixing layer as the vertical integral of $X_{P_{max}}$.

In general, $\langle X_P \rangle$ is an independent mix measure which complements the mixed and pure fluid quantities and indicates the average mole fraction of the fully mixed fluid. Near the edges of the RT layer, the amount of product $\langle X_P \rangle$ is related to the density average so that the layer width based on the $\langle X_P \rangle$ profile is the same as that based on the $\bar{\rho}$ profile. As $\langle X_P \rangle$ varies between 0 (for no mixing) and 1 (for complete mixing), it can also be used as a mix progress variable.

General comment on RT layer mixing prediction

The limitations of assessing the mixing state based on lower-moment metrics such as θ are easily seen: across the layer, θ is approximately constant not in any way
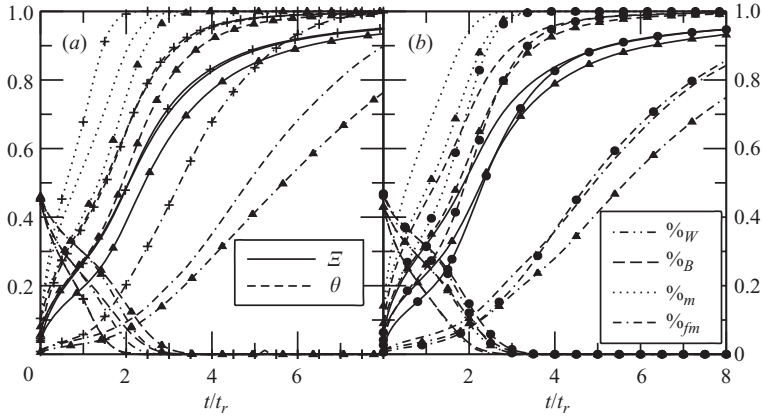
FIGURE 3. Comparison of the mix metrics for cases (*a*) 1Fr (pluses), 3Base (no symbols) and 3Sc2 (triangles) and (*b*) 2Base (no symbols), 2Sc2 (triangles) and 2Re1 (circles).

giving a notion of the radically different amounts of white, black or grey. For example at the top of the layer, the density PDF is spiked at the black end and includes some grey. In the centre of the layer, the density PDF is quasi-Gaussian and the fluid grey. At the bottom of the layer, the PDF is spiked at the white end with some grey. Such PDF characteristics are seen in the coarse-grained simulations of Youngs (1994) and Linden *et al.* (1994) and experimentally by Wilson & Andrews (2001). In short, there is no connection between θ and the local pure or mixed fluid.

3.5. *Pure-fluid fraction*

Most mix measures currently used in the RT literature attempt to indicate (unsuccessfully, as is further demonstrated) how much mixing has taken place or perhaps how much is left before the fluid is homogeneous. It is also useful to know the amount of pure fluid present and how it might be predicted or bounded by low-order moments of the PDF. The pure fluid is usually defined as having a density within 5% of either pure fluid under consideration, i.e. the pure heavy fluid has a density higher than $\rho_B = \rho_2 - 0.05(\rho_2 - \rho_1)$ and the pure light fluid has a density below $\rho_W = \rho_1 + 0.05(\rho_2 - \rho_1)$. Although the discussion below uses this value, the methodology and the conclusions are general.

Figure 3 compares Ξ, θ, the percentage of mixed fluid, $\%_m$, fully mixed fluid, $\%_{fm}$, and the percentage of pure heavy, $\%_B$, and light, $\%_W$, fluids. Note that $\%_m + \%_B + \%_W = 1$, and $\%_m = \%_{fm} + \%_{pm}$, where $\%_{pm}$ is the percentage of partially mixed fluid. In the interior of the RT layer and the present simulations, $\%_m$ is always greater than Ξ. This is because $\%_m$ counts the excess reactant in the regions where X_e is less than the pure fluid value. Conversely, Ξ or $\langle X_P \rangle$ is always larger than $\%_{fm}$. Consistent with the explanation above, $\theta \geqslant \Xi$ ($\theta = \Xi$ iff $t = 0$, inf) and θ always overpredicts the mixed fluid. Figure 3 shows that, in general, there is no connection between θ and $\%_{fm}$, $\%_m$, $\%_W$ or $\%_B$. In addition, θ is related to the variance of the excess fluid, (3.9), and does not predict the average of fully mixed fluid, $\langle X_P \rangle$, nor the percentages of mixed, fully mixed or pure fluid. This is clearly seen in figure 3; there is no pure fluid left long before the mixing process decays and $\theta = 1$. The amount of pure fluid is determined by the tails of the density distribution and, thus, cannot be predicted by measures such as Ξ or θ that are related to the low-order moments of the density distribution.

Figure 3(a) also shows that at higher A, the pure light- and heavy-fluid evolutions become different, with the pure light fluid disappearing faster than the pure heavy fluid (see cases 3Base and 3SC2). This an important VD effect, not seen in the Boussinesq case, and is examined below. The evolutions of the pure light and heavy fluid are about the same for low A cases, irrespective of the value of Re_{b_0} (see case 1Fr). The buoyancy Reynolds number collapse the evolutions of θ and $\varXi$, indicating that low-order moments of the density PDF behave similarly in the variable density and Boussinesq cases (after proper scaling).

3.6. *Bounds for pure and mixed fluids based on mix measures*

To emphasize that the usual mix measures do not predict $\%_W$, $\%_B$, $\%_m$ or $\%_{fm}$, rigorous quantitative bounds are derived. These bounds can be used to characterize the fluid composition or as realizability constraints in low-dimensional models, when low-order moments of the density PDF may be the only information available. The bounds derived below are formally the same for the two pure fluids as the usual mix measures use second-order moments and they cannot detect the PDF asymmetry which occurs in VD mixing.

Bounds on pure and mixed fluids given $\bar{\rho}$ and θ

The density PDF corresponding to the smallest and largest amounts of pure fluid is discrete, but depending on the values of $\bar{\rho}$ and θ can have values in several different points. A simple case, which is probably most relevant in practice, is when $\bar{\rho} < \rho_B$ and $\langle \rho^2 \rangle < (\bar{\rho} - \rho_1)(\rho_B - \bar{\rho})$ (equivalently $\theta > (\rho_2 - \rho_B)/(\rho_2 - \bar{\rho})$). Using the definition of ρ_B, the second condition is $\theta > 0.1$. The sample space of the ensemble with the maximum number of pure heavy fluid events is $\{\bar{\rho} - \langle \rho^2 \rangle / (\rho_B - \bar{\rho}), \rho_B\}$. The minimum number of pure heavy fluid points is zero and corresponds to density and normalized variance events clustered around $\bar{\rho}$ and θ. Given the values of $\bar{\rho}$ and θ, the percentage of black fluid is between the bounds:

$$0 \leqslant \%_B \leqslant \frac{(1-\theta)\langle \rho^2 \rangle_{nm}}{(\rho_B - \bar{\rho})^2 + (1-\theta)\langle \rho^2 \rangle_{nm}}, \tag{3.17}$$

with similar inequalities for the light fluid. Here and near the centreline of the RT layer, (3.17) reduces to:

$$0 \leqslant \%_B \leqslant \frac{1-\theta}{1.81-\theta}, \tag{3.18}$$

and is independent of the Atwood number. Similar formulae can be obtained for the amount of mixed fluid. A simple case is when $\rho_W < \bar{\rho} < \rho_B$ and $\langle \rho^2 \rangle < (\bar{\rho} - \rho_W)(\rho_B - \bar{\rho})$. Using the definitions of $\rho_W (\rho_B$ the second condition becomes $\theta > 0.19$), the maximum fraction of mixed fluid points is 1. The minimum number of mixed fluid points corresponds to the density PDF consisting of the events $\{\rho_W, (\rho_+ \rho_B)/2, \rho_B\}$, so that

$$4 \frac{-(1-\theta)\langle \rho^2 \rangle_{nm} + (\bar{\rho} - \rho_W)(\rho_B - \bar{\rho})}{(\rho_B - \rho_W)^2} \leqslant \%_m \leqslant 1, \tag{3.19}$$

which, for the homogeneous case or the interior of the RT layer, becomes

$$\frac{\theta - 0.19}{0.81} \leqslant \%_m \leqslant 1. \tag{3.20}$$

For $\theta = 0.8$ (e.g. Dalziel *et al.* 1999), it yields $0 \leqslant \%_B \leqslant 0.2$ and $0.75 \leqslant \%_m \leqslant 1.0$; for $\theta = 0.6$ we obtain $0 \leqslant \%_B \leqslant 0.33$ and $0.51 \leqslant \%_m \leqslant 1.0$.

Bounds on pure and mixed fluids given $\bar{\rho}$ and $\langle X_P \rangle$

If $X_P \leqslant 0.1$ and $\bar{\rho} < \rho_B$, then the sample space of the ensemble with the maximum number of $\rho \geqslant \rho_B$ points (pure heavy fluid) contains only the three events $\{\rho_1, (\rho_1 + \rho_2)/2, \rho_B\}$. The minimum number of pure heavy fluid (black) points is zero and all events are clustered around $\bar{\rho}$ and $\langle X_P \rangle$ values. This yields the bounds

$$0 \leqslant \%_B \leqslant \frac{2(\bar{\rho} - \rho_1)/(\rho_2 - \rho_1) - \langle X_P \rangle}{2(1 - 2(\rho_2 - \rho_B)/(\rho_2 - \rho_1))}, \tag{3.21}$$

with similar inequalities for the light fluid. Any value for $\%_B$ between the bounds is possible based on the constraints considered. For example, if $\bar{\rho} = (\rho_1 + \rho_2)/2$, corresponding to the inner region of the RT layer and the present simulations, using the definition of ρ_B the right bound becomes $(1 - \langle X_P \rangle)/1.8$. For $\langle X_P \rangle = 0.8$, it yields $0 \leqslant \%_B \leqslant 0.11$. For $\langle X_P \rangle = 0.6$, $0 \leqslant \%_B \leqslant 0.22$.

Similarly, bounds can be found for the percentage of mixed fluid, when $\bar{\rho}$ and $\langle X_P \rangle$ are known. Assuming that $\langle X_P \rangle > 0.1$ and $\rho_W < \bar{\rho} < \rho_B$, the sample space of the ensemble with the minimum number of $\rho_W < \rho < \rho_B$ mixed fluid events contains only the three possible events $\{\rho_W, (\rho_1 + \rho_2)/2, \rho_B\}$, while the maximum value for $\%_m$ is 1. Thus,

$$\frac{\frac{1}{2}(\rho_2 - \rho_1)(\rho_B - \rho_W)(\langle X_P \rangle - 1) + (\rho_B - \rho_0)(\bar{\rho} - \rho_W) + (\rho_0 - \rho_W)(\rho_B - \bar{\rho})}{2(\rho_0 - \rho_W)(\rho_B - \rho_0)} \leqslant \%_m \leqslant 1, \tag{3.22}$$

where $\rho_0 = (\rho_1 + \rho_2)/2$. For this flow or interior of the RT layer, the left inequality becomes $(\langle X_P \rangle - 0.1)/0.9 \leqslant \%_m$. For $\langle X_P \rangle = 0.8$, it yields $0.78 \leqslant \%_m \leqslant 1.0$. For $\langle X_P \rangle = 0.6$, $0.56 \leqslant \%_m \leqslant 1.0$.

3.7. *The density probability density function*

The density PDF is essential to understanding the mixing state. The mix measures described above are low-order integrals of the PDF. Figure 4 shows the density PDF at select times according to the values of the different mix measures. There are two items that are noteworthy and even surprising and will be discussed in more detail:

(i) Even though the simulations were started with equal amounts of pure fluid, the PDF is rapidly skewed at high Atwood numbers. The distribution is symmetrical for low Atwood numbers.

(ii) There is no unique connection between θ, $\varXi$, $\theta_{\rho v}$ and the underlying physical mixing state as indicated by the density PDF. The metric $\theta_{\rho v}$, based on $\langle \rho v \rangle$, is discussed below.

Figure 4 shows that the density PDF starts as symmetric double-delta corresponding to two pure fluids at the outset (modulo initial diffusion layers). As the fluids start mixing the PDF becomes very asymmetric for the higher A cases.

The density PDF evolution does not collapse with Re_{b_0}, unlike the collapse of the low-order moments θ and $\varXi$. The shape of the PDF is qualitatively different at low and high A numbers and cannot be captured by a rescaling of the rest of the parameters considered. Later, as density events far from the mean become rare, the flow becomes Boussinesq-like and the PDF takes a symmetric quasi-Gaussian shape. At high Atwood numbers, large-density events are more frequent than low-density events. The rate of mixing at high Atwood numbers is very different, depending on whether the light or the heavy fluid is sampled: pure light fluid mixes faster than the pure heavy fluid.
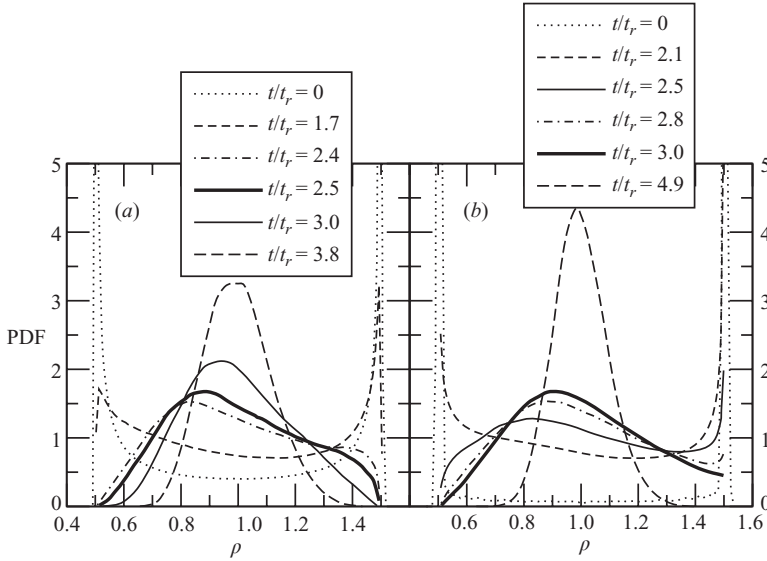
FIGURE 4. Density PDF at different times for (*a*) case 3Base and (*b*) case 3Sc2. The non-dimensional times $t/t_r = 0$, 1.7, 2.4, 2.5, 3.0 and 3.8 in (*a*) and $t/t_r = 0$, 2.1, 2.5, 2.8, 3.0 and 4.9 in (*b*) correspond to $\%_m = \theta_{\rho v} = \theta = \varXi = 0.8$. The thick lines give the PDF when $\theta = 0.8$ for two different simulations at two different times $t/t_r = 3.0$ for case 3Sc2 and at $t/t_r = 2.5$ for case 3Base. The PDFs are normalized such that the density varies between 0 and 1.

The mix metrics studied vary from zero to unity and are commonly thought of as indicating the amount of mixing that has occurred. While low-order moments, like θ, are obtained from the PDF, the shape of the PDF cannot be inferred from such measures. Nor, as can be seen in figure 4, does the state of the mixing, as predicted by similar values of the mix metrics, correspond to the same PDF. Figure 4 compares the density PDFs at the times when $\%_m = \theta = \varXi = \langle X_P \rangle = \theta_{\langle \rho v \rangle} = 0.8$. The PDF is still bi-modal when the partially mixed fluid $\%_m$ covers 80% of the field. The PDF is no longer bi-modal when $\theta_{\rho v} = \theta = 0.8$ and when $\varXi = 0.8\%$, the PDF is quasi-Gaussian.

The values of θ_∞ in the various RT experiments referenced above vary between 0.6 and 0.8. Intermediate time values are typically lower than the asymptotic ones. The PDFs for several simulations for which $\theta = 0.65$, a value more representative for the laboratory RT layer, are given in figure 5. In general, there is no correlation between θ and the PDF shape. It is seen that the same value of $\theta = 0.65$ can include mix states that contain either one or both pure fluids or neither pure fluid. At high *A*, the PDF shape and skewness and existence of either pure fluids is sensitive to both Re_0 and *Sc*, while at low *A* the PDF is symmetrical for values of Re_0, *Sc* and *Fr* considered.

The asymmetry of the density PDF in the VD case is understood from the equation for the skewness, $S \equiv \langle \rho^3 \rangle / (\langle \rho^2 \rangle^{3/2})$. Using (4.5) and

$$\frac{\mathrm{d}}{\mathrm{d}t} \langle \rho^3 \rangle = -\frac{3}{2ReSc} \langle \rho(\rho_{,j})^2 \rangle. \tag{3.23}$$

we obtain:

$$\frac{\mathrm{d}}{\mathrm{d}t} S = -S \frac{\varepsilon_\rho}{\langle \rho^2 \rangle} - \frac{3}{4} \frac{\langle \rho(\rho_{,j})^2 \rangle}{\langle \rho_{,k}\rho_{,k} \rangle \langle \rho^2 \rangle^{1/2}}. \tag{3.24}$$
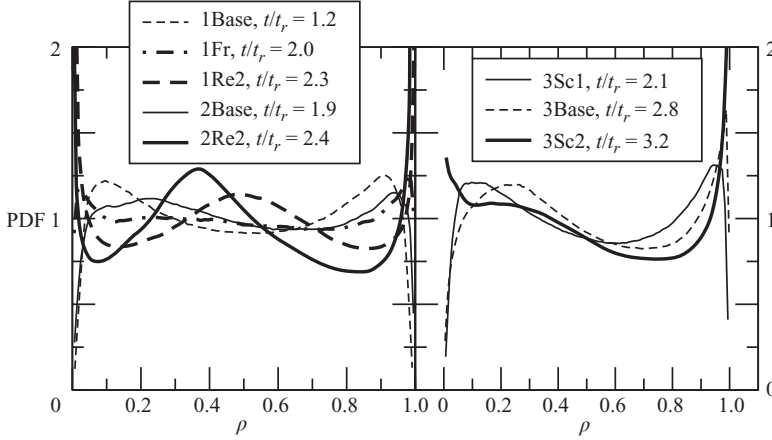
FIGURE 5. Density PDF at the time when $\theta = 0.65$ for different simulations. The PDFs are normalized such that the density varies between 0 and 1.

As the flow begins with $S = 0$, it is the second term, the production, that generates the skewness of the PDF. The quantity $\langle \rho(\rho_{,j})^2 \rangle$ is weighted towards large squared density gradient events occurring in lower than average density regions so that $S > 0$ at early times. In other words, the light fluid blobs become more fragmented at higher A. As the mixing proceeds, the production term approaches zero and we obtain a simple decay. Thus, at long times, the source term vanishes and the decay term dominates, producing a relaxation to a symmetric PDF on the density eddy turnover time scale.

For the Boussinesq case, the first important moment past the variance is the kurtosis, K_ρ. Ristorcelli & Clark (2004) monitor the evolution of the density PDF at the centreline of the Boussinesq RT layer using the density kurtosis. For the initial mixture of pure fluids the kurtosis is close to one, $K_\rho \sim 1$. The PDF becomes Gaussian-like with $K_\rho = 3$ after passing through $K_\rho = 1.8$. $K_\rho = 1.8$ corresponds to a uniform distribution which is observed only in the Boussinesq case. For a VD flow, the PDF never attains a uniform distribution, even when $K_\rho \sim 1.8$. From figure 6, it seems that the influence of A, Re_0 and Fr on the evolution of K_ρ is captured by Re_{b_0}, similar to the other lower-order moments studied. Also, at least at earlier times, the change in the evolution of K_ρ decreases as Re_0 increases, suggesting a limiting behaviour at high Reynolds numbers. If $K_\rho \to 3$ is taken to indicate the rate at which the PDF becomes Gaussian-like, then from figure 6 it seems that this decreases with Re_{b_0} or Sc. At early times, Re_{b_0} has the opposite influence. Nevertheless, it is shown below that even when the PDF is Gaussian-like, there can still be non-Boussinesq effects.

The equation for the density PDF can be derived following standard procedures (Pope 1985):

$$\frac{\partial f}{\partial t} = -\frac{1}{ReSc} \frac{\partial}{\partial \hat{\rho}} \langle \rho_{,jj} |_{\rho=\hat{\rho}} \rangle f].$$

$$(3.25)$$

Here, $\hat{\rho}$ is the sample space variable and f is the PDF. The PDF equation is, surprisingly, the same as that for the Boussinesq case, indicating that dilatational effects do not explicitly affect the density PDF. The density gradients, however, do vary substantially with the Atwood number. There are implicit dilatational effects on
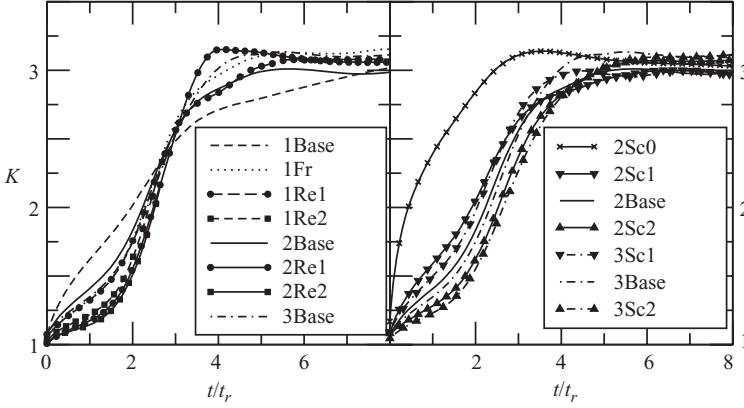
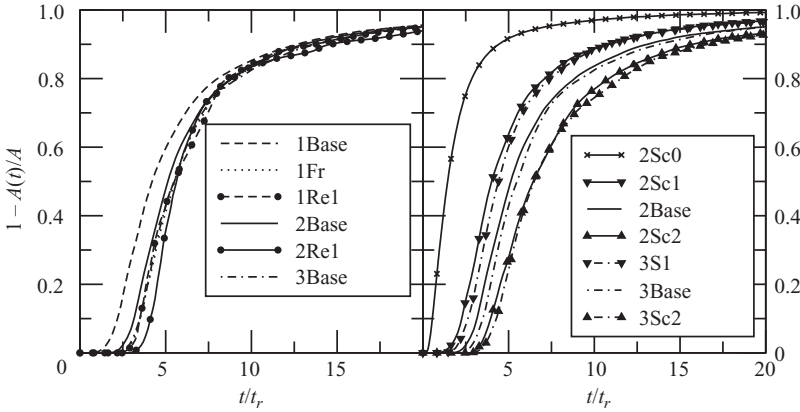FIGURE 6. Time variation of the density kurtosis.

FIGURE 7. Mixing progress as measured by the evolution of the normalized current Atwood number.

the density gradient field. Explicit dilatational effects play a role on the mixing rate, as will be seen.

3.8. *The current Atwood number*

The buoyancy force is proportional to the density differences between different regions of the flow. A local Atwood number is sometimes used as a measure suggestive of the current buoyancy force. In the present context the maximum and minimum density values in the field can be used to define an instantaneous Atwood number:

$$A(t) = \frac{\rho_{\max} - \rho_{\min}}{\rho_{\max} + \rho_{\min}}, \tag{3.26}$$

where $\rho_{\max} = \rho_{\max}(t)$ and $\rho_{\min} = \rho_{\min}(t)$ are normalized by the initial value and plotted in figure 7. The time when $A(t)$ departs from its initial value signals the disappearance of at least one of the pure fluids. The effective Atwood number is therefore based on the width of the density PDF in contradistinction to the variance which is more suggestive of the average buoyancy forces associated with the central portions of the distribution.

Note that the kinetic energy, E_K, peaks at about $t/t_r = 2.5$ (LR), and that E_K has already undergone a significant increase before a sizeable decrease in the effective
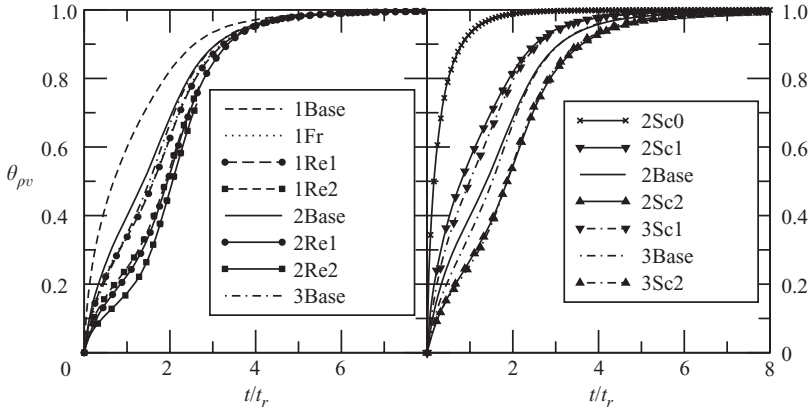
FIGURE 8. Mixing progress as measured by the evolution of the normalized density specific volume correlation, $\theta_{\rho v} = 1 - \langle \rho v \rangle / \langle \rho v \rangle |_{t=0}$.

Atwood number is obtained. There is still pure fluid for the high Re_{b_0} case at the time of the peak of the energy and turbulent Reynolds number. As we might expect, $A(t)$ is Schmidt-number sensitive. At long times, cases with the same Sc collapse; Sc appears to be the only parameter setting the long-term mixing rate.

The instantaneous Atwood number defined above is related to the time-dependent A used by George & Glimm (2005) and Liu *et al.* (2006) to collapse the growth rates obtained in RT experiments. Thus, a local Atwood number is defined using the largest and smallest (or the average 50% top largest and smallest) density values in each horizontal plane. This local Atwood number is integrated in the vertical direction and doubly integrated in time to replace At^2 in the self-similar growth rate formula $h = \alpha g At^2$. For the present simulations, the time-dependent A defined by George & Glimm (2005), $A'(t)$, behaves similarly to the instantaneous Atwood number, $A(t)$ (not shown). As a result, in unscaled time, the quantity $2 \int_t \int_s A'(s_1) ds_1 ds$, decreases with Sc and Re_0 and increases with A and $1/Fr^2$. In scaled time, the double integral remains the same if A/Fr^2 is the same.

3.9. *Density specific volume covariance,* $\langle \rho v \rangle$

The quantity $\langle \rho v \rangle$ mediates the production of the mass flux in VD turbulence, see §4. As the mass flux dictates the conversion rate of potential to kinetic energy (LR) it follows that $\langle \rho v \rangle$ is directly involved in the energy conversion. Because of the dynamical importance of $\langle \rho v \rangle$ in the mass flux equations, it appears useful and convenient to investigate its use as a measure of the mixing state. Like $\langle \rho^2 \rangle$, the covariance, $\langle \rho v \rangle$, is always single-signed (see LR). A different proof has also been given in Besnard *et al.* (1992):

$$-\langle \rho v \rangle = -\langle \rho v^* \rangle = -\langle \rho \bar{\rho} v^* \rangle / \bar{\rho} = -\langle \rho (\rho^* - \rho) v^* \rangle / \bar{\rho} = \langle \rho^2 v^* \rangle / \bar{\rho} > 0. \quad (3.27)$$

In addition, $\langle \rho v \rangle = 0$ corresponds uniquely to the fully mixed state; thus $\theta_{\rho v} = 1 - \langle \rho v \rangle / \langle \rho v \rangle |_{t=0}$ is a mix progress variable. Figure 8 shows the evolution of $\theta_{\rho v}$. In scaled time, molecular mixing is slower for cases with larger Re_{b_0} or higher Sc numbers, contributing to faster increase in the magnitude of the mass flux and faster conversion of potential to kinetic energy. In general, the collapse of $\theta_{\rho v}$ is similar to the other lower-order moments.
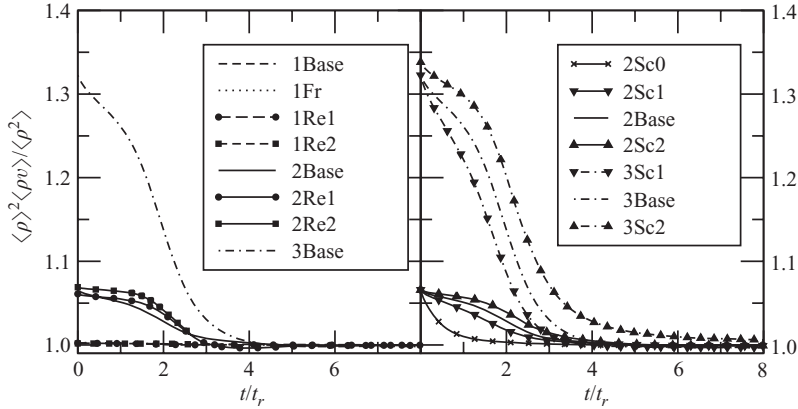
FIGURE 9. Density specific volume correlation normalized by the density variance.

3.10. *Non-Boussinesq effects and the independence of $\langle \rho v \rangle$ and $\langle \rho^2 \rangle$*

The density variance does not appear in the moment equations (§4) of a VD fluid while $\langle \rho v \rangle$ does. In a VD fluid without molecular mixing, $\langle \rho^2 \rangle$ and $\langle \rho v \rangle$ are simply related:

$$\langle \rho^2 \rangle_{nm} = (\rho_2 - \bar{\rho})(\bar{\rho} - \rho_1), \qquad \langle \rho v \rangle_{nm} = -\frac{(\rho_2 - \bar{\rho})(\bar{\rho} - \rho_1)}{\rho_1 \rho_2} = -\frac{\langle \rho^2 \rangle_{nm}}{\rho_1 \rho_2}. \quad (3.28)$$

The relation above holds, to a good approximation, for the initial values given in table 1. In the presence of molecular mixing, there is, however, no simple one to one relation between $\langle \rho^2 \rangle$ and $\langle \rho v \rangle$; this is because of the connection of $\langle \rho v \rangle$ to the mean specific volume. Taking moments of the Taylor series of $v = v(\rho)$ about $v^* = V$, it is straightforward to show that

$$\langle \rho v \rangle = -\frac{\langle \rho^2 \rangle}{\bar{\rho}^2} \left[1 - i_\rho \frac{\langle \rho^3 \rangle}{\langle \rho^2 \rangle^{3/2}} + i_\rho^2 \frac{\langle \rho^4 \rangle}{\langle \rho^2 \rangle^2} - i_\rho^3 \frac{\langle \rho^5 \rangle}{\langle \rho^2 \rangle^{5/2}} + \cdots \right] \qquad \left(i_\rho = \frac{\langle \rho^2 \rangle^{1/2}}{\bar{\rho}} \right). \quad (3.29)$$

Keeping only the first term, we obtain the relationship for the Boussinesq case. For the VD case, We need all the moments of the density PDF in order to determine $\langle \rho v \rangle$. The normalized moments are usually of order one and the series converges slowly for large A, for which $i_\rho \sim 1$. For a Gaussian (or, more generally, symmetric) PDF, the odd terms are all zero and $\langle \rho v \rangle$ always has larger magnitudes than $\langle \rho^2 \rangle / \bar{\rho}^2$. For highly skewed fields, as occurs on either side of the RT layer (Ristorcelli & Clark 2004), the second term becomes important.

Figure 9 compares the density volume covariance with the density variance. The ratio is seen as indicative of VD effects since the two quantities behave the same for the Boussinesq case. Thus, it increases with the (effective) Atwood number, Re_0, or Sc and becomes small for small density intensities.

3.11. *Bounds for pure and mixed fluids based on $\theta_{\rho v}$*

Based on the values of $\bar{\rho}$ and $\theta_{\rho v}$ we can derive bounds for the allowed values of the percentage of pure and mixed fluids. Assuming for simplicity that $\bar{\rho}$ and V are outside the pure heavy fluid values (i.e. $\bar{\rho} < \rho_B$ and $V > 1/\rho_B$ which leads to $1 - (1 - \theta_{\rho v}) \langle \rho v \rangle_{nm} > 1/\rho_B$), the sample space of the ensemble with the maximum number of pure heavy fluid events is comprised of only the events $\{(\rho_B - \bar{\rho})/(\rho_B V - 1), \rho_B\}$. The minimum number of pure heavy fluid points is zero as the instantaneous values of

density and specific volume can be clustered around $\bar{\rho}$ and $V = 1 - (1 - \theta_{\rho v})\langle \rho v \rangle_{nm}$. Thus, the percentage of black fluid is bounded by:

$$0 \leqslant \%_B \leqslant \frac{\rho_B V(\bar{\rho}V - 1)}{\bar{\rho}V - 1 + (\rho_B V - 1)^2}, \tag{3.30}$$

with similar inequalities for the light fluid. Near the centreline of the RT layer and for the present simulations, (3.30) becomes:

$$0 \leqslant \%_B \leqslant \frac{(1 + 0.9A)V(V - 1)}{V - 1 + ((1 + 0.9A)V - 1)^2}, \tag{3.31}$$

with $V = (1 - \theta_{\rho v}A^2)/(1 - A^2)$. Similar bounds can be found for $\%_m$ by searching for the density PDF distributions which give the maximum and minimum amounts. For $\bar{\rho}$ and V outside the pure fluid values, the sample space events $\{\rho_W, \sqrt{\rho_W \rho_B}, \rho_B\}$ give the minimum value for the amount of mixed fluid leading to:

$$\frac{\rho_W + \rho_B - \bar{\rho} - V\rho_W\rho_B}{\left(\sqrt{\rho_B} - \sqrt{\rho_W}\right)^2} \leqslant \%_m \leqslant 1, \tag{3.32}$$

which for the present flow and interior of the RT layer becomes

$$\frac{1 - V(1 - 0.81A^2)}{(\sqrt{1 + 0.9A} - \sqrt{1 - 0.9A})^2} \leqslant \%_m \leqslant 1. \tag{3.33}$$

Unlike the bounds based on $\bar{\rho}$ and θ, in this case the dependence on A is retained. For $\theta_{\rho v} = 0.8$ and $A = 0.25$, it yields $0 \leqslant \%_B \leqslant 0.23$ and $0.74 \leqslant \%_m \leqslant 1.0$; for $A = 0.5$, it yields $0 \leqslant \%_B \leqslant 0.28$ and $0.7 \leqslant \%_m \leqslant 1.0$

4. Mixing rate

The feedback between the density and velocity fields in buoyantly driven VD turbulence is illustrated. The moment equations that describe the evolution of the statistics of the flow are used to explain the inter-relationship between molecular scalar mixing, the stirring by fluctuating strain field and the generation of kinetic energy. Phenomenological issues related (i) to PDF of the density gradients and their relation to the mixing rate and (ii) the scaling of the stoichiometric surface area, are presented. The eddy turnover length- and time-scale ratios of the density and velocity fields are presented to explore the relevance of the usual Boussinesq case closure notions for the VD mixing rate.

4.1. *Equations of buoyantly driven VD mixing*

Active scalar mixing can be described by measures related to the evolution of the scalar fields from initially segregated materials with double delta PDF to a molecularly mixed fluid with a quasi-Gaussian PDF. This evolution is most simply discussed using the second moment equations:

$$\bar{\rho}\frac{\mathrm{d}}{\mathrm{d}t}\tilde{k} = a_i P_{,i} + \langle pd \rangle - \langle u_{i,j}\tau_{ij} \rangle, \tag{4.1}$$

$$\bar{\rho}\frac{\mathrm{d}}{\mathrm{d}t}a_i = -\langle \rho v \rangle P_{,i} + \bar{\rho}\langle vp_{,i} \rangle - \bar{\rho}\langle u_i d \rangle, -\bar{\rho}\varepsilon_i, \tag{4.2}$$

$$\frac{\mathrm{d}}{\mathrm{d}t}\langle \rho v \rangle = -2\bar{\rho}\langle vd \rangle = -2\bar{\rho}\varepsilon_{\rho v}. \tag{4.3}$$

Here $2\bar{\rho}\tilde{k} = R_{nn} = \bar{\rho}\langle u_k u_k \rangle - \bar{\rho}a_k a_k + \langle \rho u_k u_k \rangle$ and $d = u_{k,k} = (1/ReSc)\,(\ln\rho)_{,kk}$. The dilatational velocity field sets the mixing rate. In a VD flow, unlike the Boussinesq case, molecular diffusion is always accompanied by a fluid particle velocity. The VD mixing rate can be written as a positive semi-definite dissipative type quantity

$$\varepsilon_{\rho v} = \frac{1}{ReSc}\left\langle \frac{\rho_{,j}}{\rho^{*3/2}}\,\frac{\rho_{,j}}{\rho^{*3/2}} \right\rangle, \tag{4.4}$$

from which we might argue that mixing takes place faster in the lower-density fluid.

Some observations regarding the coupling of this VD system may be useful. The mass flux, which mediates the transfer between potential and kinetic energies (LR), determines the production of the kinetic energy, which stirs the fluid, (4.1). The mean pressure gradient modulated by $\langle \rho v \rangle$ generates the mass flux (4.2). Thus, $\langle \rho v \rangle$, which is determined by the mixing state, sets the stirring rate. For the Boussinesq case, the role of $\langle \rho v \rangle$ in generating the mass flux is played by $\langle \rho^2 \rangle$ and the mean pressure gradient is replaced by the hydrostatic head in the mass flux equation. Because of its connection to the dynamics of the stirring in the presence of a pressure gradient and because it vanishes when the mixing is completed, it appears useful to use $\langle \rho v \rangle$ as a measure of the mixing state for VD flows, as considered above.

The absence of a one to one connection between $\langle \rho v \rangle$ and $\langle \rho^2 \rangle$ is suggested by the mechanisms by which they are mixed. In contrast to $\langle \rho v \rangle$ (4.4), $\langle \rho^2 \rangle$ is atomically mixed by the same mechanism as in the Boussinesq case:

$$\frac{\mathrm{d}}{\mathrm{d}t}\langle \rho^2 \rangle = -\mathscr{D}\langle \rho_{,j}\rho_{,j} \rangle = -2\varepsilon_\rho. \tag{4.5}$$

This, again, highlights the difference between VD and Boussinesq mixing and underscores the importance of the dilatational field in setting the mixing rate for the VD case.

4.2. *Probability density function of the density gradient*

The rate at which molecular mixing occurs, $\varepsilon_{\rho v}$ (4.4), depends on the width of the diffusion layers between the two fluids and can be assessed by the steepness of the density gradients. Figure 10 shows the typical PDFs of the scaled density derivative, $\rho_{,j}/\rho^{*3/2}$ in horizontal and vertical directions at different times.

The field is initially composed of regions of pure fluids, in which the density derivative is zero except in thin mixing layers between the two fluids. This corresponds to a PDF in which events near zero occur with highest frequency and large events occur with low frequency (figure 10). The large initial density gradients are rapidly smoothed by diffusion as indicated by the reduction of the width of the PDF at $t/t_r = 0.5$. As turbulent fluctuations grow, stirring brings together unmixed regions of fluid, stretching, folding and compressing the diffusion layer. The PDF then becomes wider by $t/t_r = 1$ and now density gradient events of magnitude larger than when the fluid was initially unmixed occur. At the same time, stirring competes with the molecular mixing which decreases density gradients and tends to narrow the PDF so, at late time, the PDF becomes narrow again.

In the vertical direction, large positive density gradient values occur more often than negative values. These events correspond to heavy over light fluid events in which the fluid blobs move towards each other. The mixing layers in between are compressed, creating larger density gradients and increasing the rate of atomic mixing. Conversely, when light fluid overlies heavy fluid, the relative compression of the diffusion layers is reduced, as the fluid blobs move less frequently towards each other. In most light over
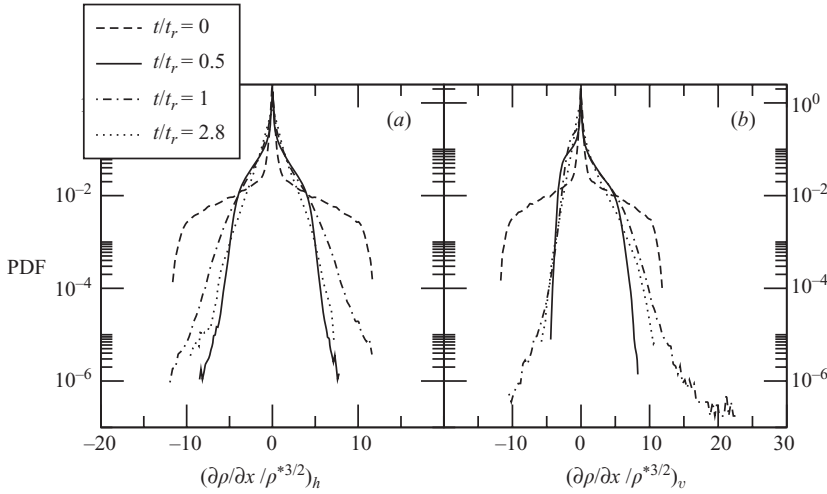
FIGURE 10. Scaled density derivative PDF at different times for case 3Base in (*a*) horizontal and (*b*) vertical directions.

heavy fluid configurations, the fluid blobs move in opposite directions, expanding the mixing layers and reducing the molecular mixing rate.

4.3. *Interfacial surface area*

The rate at which the mixing progresses depends on the steepness of the density gradients and also on the mixing-layer surface area. Material iso-concentration surfaces stretched, rotated and folded by velocity gradients are smoothed out, preferentially in large-curvature regions, by diffusion (Pope 1988). In a RT configuration, knowledge about the iso-concentration surfaces can be used to characterize the extent of the mixing layer, properties and location of the layer front, and also the mixing state and progress. For example, the variation of the area of the iso-density surfaces defined by $\rho^* = \rho_W$ and $\rho^* = \rho_B$, gives information about the evolutions of the pure heavy and light fluid front.

The area of the $\rho^* = \rho_a$ iso-density surface, $\Sigma(\rho_a)$, in a control volume, can be calculated as the product of the average density gradient magnitude evaluated at $\rho = \rho_a$ and the density PDF (Vervisch *et al.* 1995):

$$\Sigma(\rho_a) = \langle |\nabla\rho|_{\rho=\rho_a} \rangle f(\rho_a). \tag{4.6}$$

The stoichiometric, $\rho^* = (\rho_1 + \rho_2)/2$ for $\nu_1 = \nu_2 = 1$, iso-density surface area per unit volume, Σ_{st}, gives information about the mixing state and progress. Cabot & Cook (2006) presented data suggesting that Σ_{st} scales with the square of the velocity Taylor microscale, λ_u in a VD RT mixing layer. The scaling appears to include contributions to the iso-density area owing to the overall growth of the mixing layer as well as to the local stirring by the fluctuating strain. For the present flow in which the total volume is constant, there is a better scaling with the inverse of the velocity Taylor microscale. However, the velocity Taylor microscale scaling does not capture the dependence of the interfacial area on the Schmidt number as might be expected from the $\lambda_u/\lambda_\rho \sim (Sc)^{1/2}$ scaling in flows with $Sc \neq 1$. For the present simulations, as suggested by (4.6), Σ_{st} scales with the inverse of the density Taylor microscale, λ_ρ, (figure 11). It is clear, pursuing the different Schmidt-number cases, that the density Taylor microscale with its dependence on the material diffusivity, is the appropriate
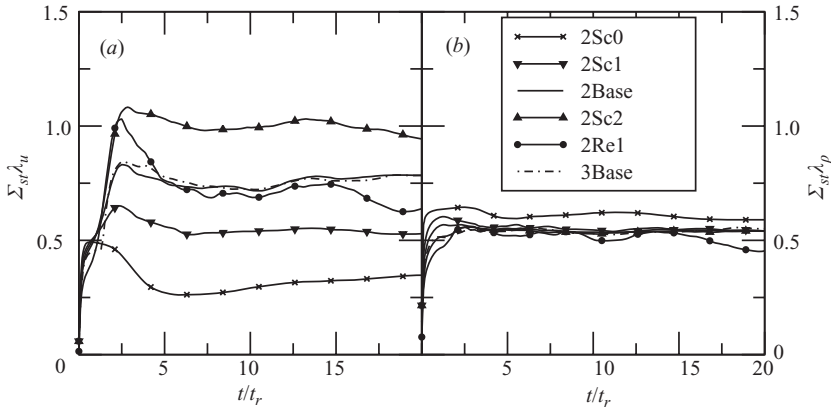
FIGURE 11. Stoichiometric iso-density surface area per unit volume multiplied by the horizontal (*a*) velocity Taylor microscale and (*b*) density Taylor microscale.

scaling for the iso-density area given the collapse of the data. Parenthetically, and in contrast to the usual Kolmogorov heuristics, the velocity and density Taylor microscale ratio varies with time and Reynolds number in non-stationary turbulence as observed in Ristorcelli & Clark (2004) and Ristorcelli (2006). Such behaviour is not consistent with either self-similarity (Ristorcelli & Clark 2004) or the scalings of fully developed turbulence. Is is not known as to whether this is a legitimate non-equilibrium effect or is due to *Re* not being high enough.

4.4. *The time scale ratio and mixing rate models*

For mixing in the Boussinesq case, the scalar and energy turnover time ratio,

$$r_B(t) = \frac{2\bar{\rho}\tilde{k}\varepsilon_\rho}{\langle \rho^2 \rangle \varepsilon} = \frac{3}{5}\frac{\lambda_u^2}{\lambda_\rho^2}\frac{1}{Sc} \tag{4.7}$$

is assumed constant (Warhaft & Lumley 1978; Livescu, Jaberi & Madnia 2000), in simple mixing rate closures for ε_ρ. See Ristorcelli (2006) for a historical summary. This is expected to be useful for passive scalar homogeneous turbulence as the influence of initial conditions vanishes. The time-scale ratio is proportional to the square of the ratio of Taylor microscales of the velocity to scalar fields. In time units scaled by k/ε, r_B is the non-dimensional mix rate (Ristorcelli 2006).

The 'Boussinesq' time-scale ratio based on the density variance is shown in figure 12. At early times, when the flow is at its most non-equilibrium, the time-scale ratio varies considerably. This is especially true for cases with higher Atwood and Reynolds numbers or smaller Schmidt numbers. In the decay stage, as the flow becomes Boussinesq-like, $r_B(t)$ becomes similar, with values around the isotropic turbulence value of 2, for the cases with $Sc = 1$.

In the VD case, the analogous time-scale ratio is

$$r_{VD}(t) = \frac{2k\varepsilon_{\rho v}}{\langle \rho v \rangle \varepsilon}. \tag{4.8}$$

Variations in $r_{VD}(t)$ are similar to those of $r_B(t)$ during the evolution of the flow (figure 13), although, quantitatively, r_{VD} and r_B are different at higher *A*. It appears that the constant-time-scale assumption is not useful, except in a rudimentary order of magnitude sense, as a closure for the scalar dissipation.
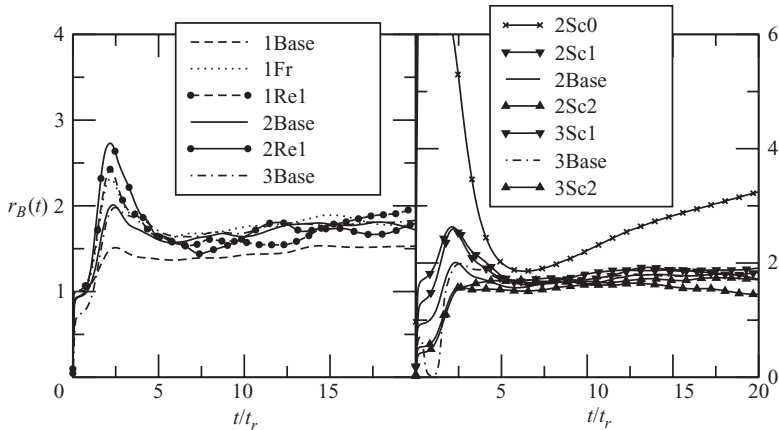
FIGURE 12. Time variation of $r_B(t)$.
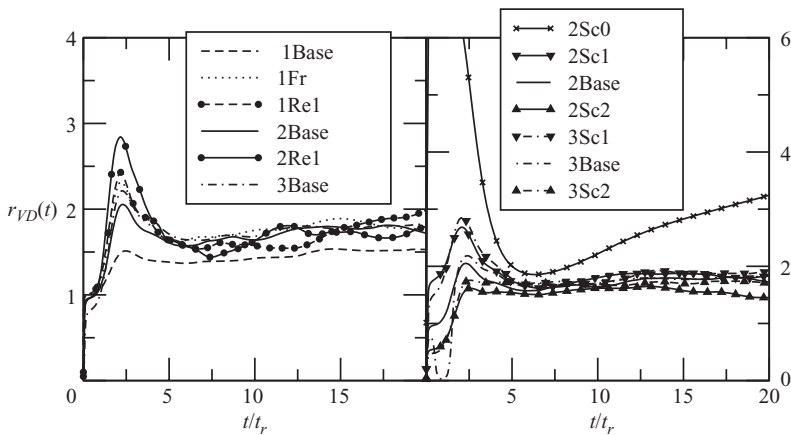
FIGURE 13. Time variation of $r_{VD}(t)$.

The ratio of integral length scales (figure 14) is used in phenomenological discussions of mixing (see references in Ristorcelli 2006). The integral length scales are computed from the κ^{-1} moment of the spectra of the velocity and density fields. As we might expect, probably owing to the coupling between material and turbulence fields in buoyantly driven flows, they are commensurate for the $Sc = 1$ cases. The cases with $Sc \neq 1$ are surprisingly different given that the integral length scale is a large-scale quantity and the only difference in the simulations is the molecular diffusion coefficient.

5. Turbulence structure

The influence of the buoyancy production mechanism on the turbulence structure is examined in both physical and spectral spaces. This is of intrinsic fluid physics interest as well as modelling interest for both LES procedures as well as single or two-point moment closures.
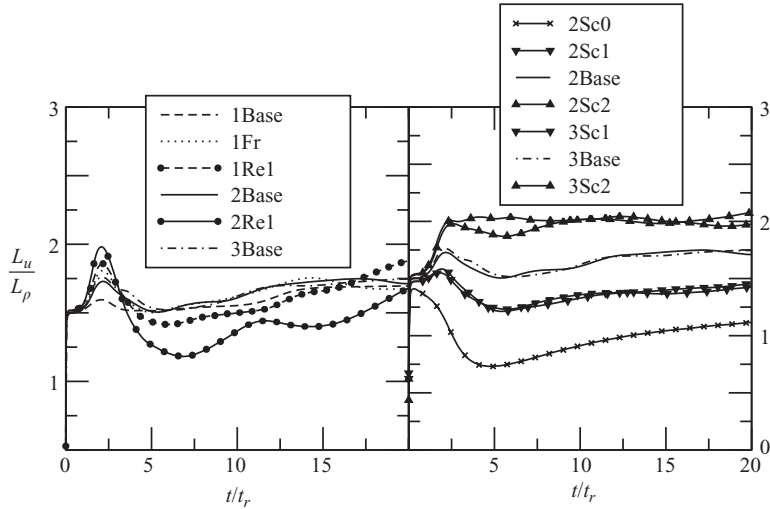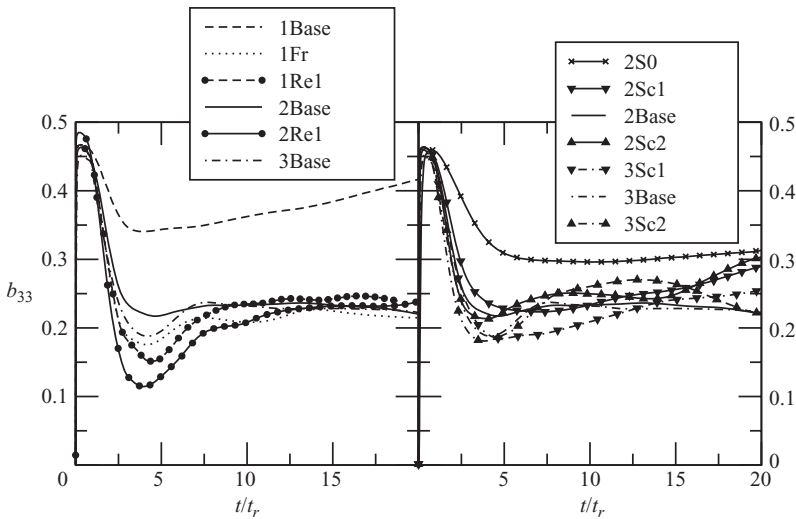
FIGURE 14. Ratio of integral length scales L_u/L_ρ.

FIGURE 15. Vertical component of the anisotropy tensor.

5.1. *Turbulence anisotropy*

Since the buoyancy production is anisotropic, the normal stresses are also anisotropic (figure 15). While the normal stresses anisotropy is large during the early stages, in the late-time decay stage, it appears that the flow reaches an equilibrium between energy production and viscous dissipation and pressure–strain redistribution so that the large scales are never isotropic. This is also seen in the Boussinesq homogeneous simulations of Batchelor *et al.* (1992) and Boussinesq RT turbulence (Cook & Dimotakis 2001; Ristorcelli & Clark 2004; Cabot & Cook 2006).

Simple dimensional arguments supported by the spectral data indicate that mass flux production becomes smaller than viscous dissipation and nonlinear transfer at small scales (see below). However, at very early times, the sudden application of the buoyancy force leads to anisotropy at all scales, as the flow is highly non-equilibrium.
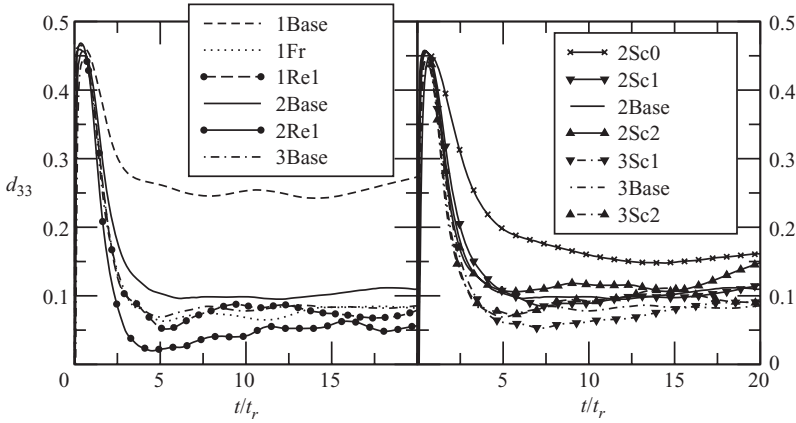
FIGURE 16. Vertical component of the dissipation anisotropy tensor.

Later, but still in the energy-growth stage, the viscous dissipation and the nonlinear terms have opposite sign and similar magnitudes so that the buoyancy production remains important at the smallest scales. It is pertinent to see if this is reflected in the anisotropy of the small scales. The dissipation (or vorticity for solenoidal velocity fields) anisotropy can be parameterized using the dissipation tensor:

$$d_{ij} = \frac{\epsilon_{ij}}{\epsilon_{kk}} - \frac{1}{3}\delta_{ij}. \tag{5.1}$$

Here ϵ_{ij} is the dissipation of the Favre Reynolds stress $\langle \rho^* u_i u_j \rangle / 2$. Figure 16 shows the evolution of the vertical component, d_{33}. The dissipation anisotropy follows the evolution of the large-scale anisotropy. It quickly increases initially and by $t/t_r = 0.2$, d_{33} reaches a peak with a magnitude slightly lower than b_{33}. Then d_{33} decreases and appears to reach an asymptotic value by $t/t_r = 5$. For cases with larger maximum Reynolds number, the asymptotic value is smaller.

In addition to the cancellation of nonlinear and viscous effects in the dissipation range mentioned above and detailed in the next section, there is another mechanism likely to contribute to the persistent anisotropy of the smallest scales. As the Kolmogorov scale grows larger in the decay stage, the influence of the anisotropy of the production occurring at larger scales is more readily felt. This can be seen clearly by comparing the vertical and horizontal longitudinal structure functions, $S_{l_v}^n = S_3^n = \langle (u_3(x_3 + r) - u_r(x_3))^n \rangle$ and $S_{l_h}^n = 1/2(S_2^n + S_1^n)$ (figure 17). Consistent with the results above, at early times S_v^2 and S_h^n are different at all scales. Later, the results at small separation distances, r, become close, but they remain clearly different at large scales. As the Kolmogorov scale grows, the dissipation scales become larger and reach separation distances at which the buoyancy production has larger magnitude.

5.2. *Spectral energy production and transfer*

Various aspects of the flow are discussed in the context of the spectra of the density and velocity fields. Two spectral length scales reflecting different dynamical balances are derived and used to discuss the associated physical processes.

At early times, the density energy spectrum maintains its initial top-hat shape (figure 18). The buoyancy production leads to a similar shape in the solenoidal energy spectrum (see below). As the large blobs are stirred by the turbulent motions, the top-hat shape disappears. As the Reynolds number increases, a modest inertial range
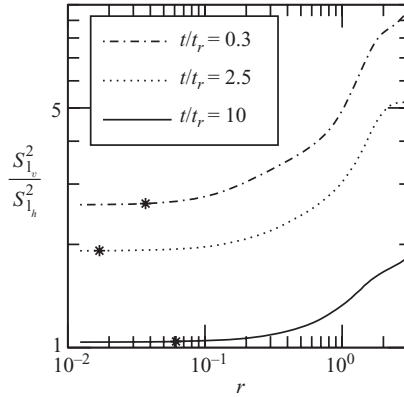
FIGURE 17. Ratio of vertical and horizontal longitudinal second-order structure functions at different times for case 2Re1. The asterisk indicates the Kolmogorov microscale.
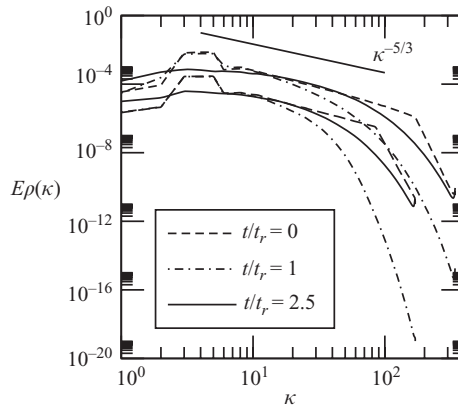

FIGURE 18. Density energy spectra at different times for cases 1Re2 (lower curves) and 2Re2 (upper curves).

appears to emerge with a $-5/3$ exponent, although it is difficult to draw definite conclusions from the data.

For VD flows, there is a difference between kinetic energy per unit mass and per unit volume. Following ideas from compressible turbulence studies (Cook & Zhou 2002; Livescu, Jaberi & Madnia 2002), the kinetic energies per unit mass and volume can be written as:

$$E_m = \tfrac{1}{2}\langle u_i u_i \rangle, \qquad E_v = \tfrac{1}{2}\langle w_i w_i \rangle, \qquad w_i = \sqrt{\rho^*} u_i. \tag{5.2}$$

The corresponding spectral forms are $\mathscr{E}_v = \langle \hat{w}_i \hat{w}_i^\dagger \rangle$, $\mathscr{E}_m = \langle \hat{u}_i \hat{u}_i^\dagger \rangle$, where $\hat{\ }$ denotes Fourier transform and $\dagger$ the complex conjugate. For the cases considered, except at very early times and at small scales, the differences between $\mathscr{E}_m$ and $\mathscr{E}_v$ are small (not shown).

The solenoidal and dilatational parts of the kinetic energy are written using the Helmholtz decomposition: w_i is divided into its compressible and divergence-free parts (Livescu *et al.* 2002). As figure 19 shows, initially the kinetic energy resides entirely in the dilatational component and its spectrum is determined by the density initialization. As the flow evolves, solenoidal energy is rapidly generated and becomes
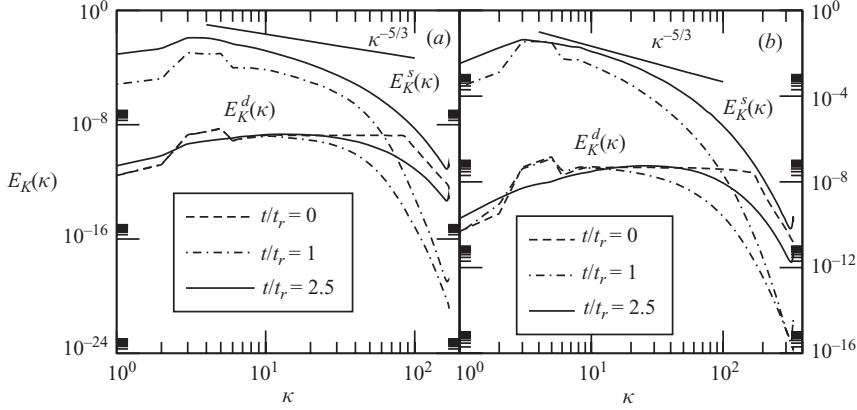
FIGURE 19. Solenoidal (upper curves) and dilatational (lower curves) energy spectra at different times for cases (*a*) 1Re2 and (*b*) 2Re2.

much larger than the dilatational part at all scales. Nevertheless, since the dilatational velocity is set by the derivatives of the density field, $\mathscr{E}_m^d(\kappa)$ decreases more slowly than $\mathscr{E}_m^s(\kappa)$ as κ increases and the relative importance of the dilatational part is larger at small scales. The solenoidal energy spectrum appears to be developing an inertial range as the Reynolds number increases to its maximum.

To investigate the mechanisms of energy growth at different scales, the spectral evolution of the energy is considered. The transport equation for w_i is derived from (2.1)–(2.3):

$$w_{i,t} = F_{vi} + N_{vi} + V_{vi}, \tag{5.3}$$

$$F_{vi} = \sqrt{\rho^*}\,\frac{g_i}{Fr^2} - \frac{1}{\sqrt{\rho^*}}P_{,i}, \tag{5.4}$$

$$N_{vi} = -(w_i u_j)_{,j} + \tfrac{1}{2}w_i u_{j,j} - \frac{1}{\sqrt{\rho^*}}p_{,i}, \tag{5.5}$$

$$V_{vi} = \frac{1}{\sqrt{\rho^*}}\tau_{ij,j}. \tag{5.6}$$

F_{vi}, N_{vi} and V_{vi} represent buoyancy production, nonlinear and viscous effects. The spectral equation for the energy per unit volume is then

$$\langle \hat{w}_i \hat{w}_i^\dagger \rangle_{,t} = \underbrace{\langle \hat{w}_i \hat{F}_{vi}^\dagger + \hat{w}_i^\dagger \hat{F}_{vi} \rangle}_{FV} + \underbrace{\langle \hat{w}_i \hat{N}_{vi}^\dagger + \hat{w}_i^\dagger \hat{N}_{vi} \rangle}_{NV} + \underbrace{\langle \hat{w}_i \hat{V}_{vi}^\dagger + \hat{w}_i^\dagger \hat{V}_{vi} \rangle}_{VV}. \tag{5.7}$$

The spectral energy per unit mass equation can be derived similarly starting from the instantaneous equations (2.1)–(2.3).

$$\langle \hat{u}_i \hat{u}_i^\dagger \rangle_{,t} = \underbrace{\langle \hat{u}_i \hat{F}_{mi}^\dagger + \hat{u}_i^\dagger \hat{F}_{mi} \rangle}_{FM} + \underbrace{\langle \hat{u}_i \hat{N}_{mi}^\dagger + \hat{u}_i^\dagger \hat{N}_{mi} \rangle}_{NM} + \underbrace{\langle \hat{u}_i \hat{V}_{mi}^\dagger + \hat{u}_i^\dagger \hat{V}_{mi} \rangle}_{VM}, \tag{5.8}$$

$$F_{mi} = \frac{g_i}{Fr^2} - \frac{1}{\rho^*}P_{,i}, \tag{5.9}$$

$$N_{mi} = -(u_i u_j)_{,j} + u_i u_{j,j} - \frac{1}{\rho^*}p_{,i}, \tag{5.10}$$

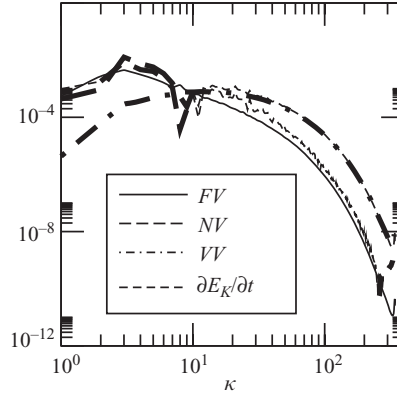$$V_{mi} = \frac{1}{\rho^*}\tau_{ij,j}. \tag{5.11}$$

FIGURE 20. Balance of the terms in spectral energy per unit volume (5.7) for case 2Re2 at an early time, before the kinetic energy peak. In order to use a logarithmic scale, only the absolute values are shown and values which are otherwise negative are plotted with thick lines.

For the cases considered, the differences between the energy per unit mass and unit volume formulations are small except at initial times when the density gradients are largest and there has been little molecular diffusion. As the density field is smoothed out by diffusion, the terms in (5.7) and (5.8) become close. Figure 20 shows the terms in (5.7) at a typical time before the kinetic energy peak.

Initially, the velocity has only a dilatational component given by (2.8). Therefore, at the initial instant the mass flux is zero, since $\langle \rho^* u_i^d \rangle = -(1/ReSc)\langle \rho^* \rho_{,i}/\rho^* \rangle = 0$. As the fluids start to move, the energy is generated at all scales by the anisotropic production term in (5.7) and at intermediate and small scales, in addition, by the nonlinear transfer term. The anisotropy generation at small scales and the subsequent isotropization, suggested by the evolution of d_{33} and the structure functions presented in the previous section, are explained below.

5.2.1. *Spectral balances and wavenumber ranges*

Two spectral length scales reflecting the different dynamical balances are now derived. Using a simple scaling argument, the critical wavenumber reflecting the balance between the buoyancy and nonlinear effects in the spectral energy per unit volume equation is obtained from the solution of:

$$\kappa_{BN} = [A/(Fr^2 \mathscr{E}_K(\kappa_{BN}))]^{1/2}. \tag{5.12}$$

Nonlinear effects dominate buoyancy effects at large wavenumbers, but only if the energy spectrum does not decay faster than κ^{-2}. Note that κ_{BN} is larger at higher Atwood numbers or smaller Froude numbers. A wavenumber scaling reflecting the balance of buoyancy and viscous forces is obtained from:

$$\kappa_{BV} = \left[Re_0 A/Fr^2 \mathscr{E}_\rho(\kappa_{BV})^{1/2}/\mathscr{E}_K(\kappa_{BV})\right]^{2/5}. \tag{5.13}$$

Viscous forces dominate the buoyancy forces for $\kappa > \kappa_{BV}$. This increases with A or Re and decreases with Fr. In the viscous range, the nonlinear and viscous terms in (5.7) have opposite signs and similar magnitudes (figure 20) and it appears that the buoyancy production, though small, has an important contribution to the left-hand side of (5.7) in this spectral range at early times. Note that as the kinetic energy grows, there is a lag between the viscous dissipation and energy production so that, at very early times, the small scales become strongly anisotropic. Later, as explained
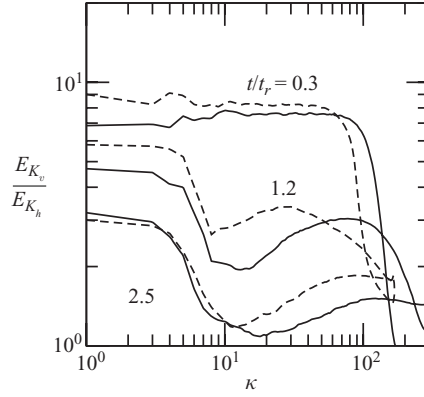
FIGURE 21. Ratio of vertical to horizontal spectral kinetic energy for cases 1Re2 (dashed lines) and 2Re2 (continuous lines) at different times.

below, as the nonlinear transfer term starts to contribute to the energy increase, the anisotropy decreases. After the initial instant, as nonlinear effects start to dominate the buoyancy production, the intermediate scales become almost isotropic. At the very small scales, however, owing to the cancellation between the nonlinear and viscous terms, the buoyancy production remains relatively important and there is a persistent small-scale anisotropy even after the dissipation overcomes production during the decay stage.

5.2.2. *Time scale of non-equilibrium spectral processes*

As the buoyancy force is applied suddenly, the buoyancy production sets the kinetic energy increase at all scales at early times and the flow becomes anisotropic at all scales (figure 21). Later, the nonlinear interactions pick up and contribute to the increase in kinetic energy at intermediate and small scales. Thus, as seen in figure 21, the anisotropy among the normal stresses decreases at these scales, consistent with the structure functions ratio and d_{33} trends. Concomitantly, the pressure–strain terms decrease the anisotropy at large scales, as seen in the b_{33} time variation. A legitimate question to ask is then how fast does the energy reach the small scales through the cascade process compared to the time scale associated with the increase in the production term. In other words, how fast does the nonlinear term increase at small scales compared to the buoyancy term.

One estimate of the energy-cascade-process time scale, τ_E, comes from Kraichnan (1971), which assumes that an eddy with wavenumber κ_0 is affected through a shearing motion by all wavenumbers smaller than κ_0:

$$\tau_E^2 \sim \left(\int_0^{\kappa_0} \mathcal{E}_K(\kappa) \kappa^2 \mathrm{d}\kappa \right)^{-1} \sim \left(\mathcal{E}_K(\kappa_0) \kappa_0^3 \right)^{-1}. \tag{5.14}$$

The production term in (5.7) increases at small scales through its cascade process. A simple estimation of the time scale, τ_B, associated with this process leads to:

$$\tau_B \sim \frac{1}{Fr^2} \left(\int_0^{\kappa_0} (\mathcal{E}_K(\kappa))^{1/2} (\mathcal{E}_\rho(\kappa))^{1/2} \kappa \, \mathrm{d}\kappa \right)^{-1} \sim \left(\mathcal{E}_K(\kappa_0) \mathcal{E}_\rho(\kappa_0) \kappa_0^4 \right)^{-1/2}. \tag{5.15}$$

Assuming that $\mathscr{E}_m$ and $\mathscr{E}_v$ have the same κ dependence and the density spectrum behaves like $\mathscr{E}_\rho \sim \kappa^{-n}$, then the ratio of the time scales is:

$$\tau_E/\tau_B \sim \frac{1}{Fr^2}\kappa^{(1-n)/2} \qquad (5.16)$$

For any Froude number, if the density spectrum is steeper than κ^{-1}, τ_E/τ_B goes to zero as $\kappa \to \infty$. In short, the rate of increase of small-scale energy is faster through nonlinear cascade processes than buoyancy production. At early times, the small scales are strongly anisotropic owing to the sudden application of the buoyancy force. Owing to the finite amount of time required for the nonlinear transfer term to start to act at progressively smaller scales, larger scales become isotropic faster, as seen in figure 21. Near the viscous range, the energy increase is retarded by an increase in the viscous dissipation and the anisotropy persists. The progressive decrease in anisotropy at intermediate wavenumbers is not seen in the ratio of the longitudinal structure functions (figure 17) as this behaviour is masked by the contribution from the single-point correlation to the structure function. A similar isotropization mechanism may occur in the inner regions of the RT layer, so that at long times, the intermediate-scale anisotropy is small. This is consistent with the high-Reynolds-number simulations of Cabot & Cook (2006). The isotropization of the intermediate scales may seem to be indicative of the emergence of an inertial range. However, this flow during the growth stage, as well as RT turbulence, is highly non-stationary with a continuous increase of energy at all scales. Therefore, the classical high-Reynolds-number picture with an inertial range in which the nonlinear transfer term is small and the viscous scales become decoupled from the large scales may not apply. The question of how an inertial range would look in buoyantly driven turbulence seems to remain open. We note, in addition, that, whenever there is a cancellation between nonlinear and viscous forces, as happens in the viscous range, or if the buoyancy effects are suddenly increased, as may happen at the edges of the RT layer or under variable accelerations, the anisotropic effects of the buoyancy production should be felt up to the smallest scales of motion.

6. Summary of findings

Simulations of the mixing produced by buoyancy-generated motions in an unstably stratified medium, as occurs in the VD RT layer, have been conducted. The medium is composed of two miscible fluids with different densities and the same diffusivities. Simulations with Atwood number in the range $0.05 \leqslant A \leqslant 0.5$, capturing the transition from Boussinesq-like evolution to important non-Boussinesq effects, are studied. The effects of molecular diffusion, as parameterized by the Schmidt number, are investigated over a twenty-fold variation, $0.1 \leqslant Sc \leqslant 2$. For the high-initial-Reynolds-number case, turbulent Reynolds numbers of the order of $Re_t = 2380$ (or $Re_\lambda = 210$ in the vertical direction) occurred in the simulations.

The VD mixing-simulation results permit several big picture fluid physics generalizations. The most unexpected and surprising result is the large skewness of the density PDF during mixing in a VD flow, not seen in the Boussinesq case: the light pure fluid mixes much more rapidly than the heavy pure fluid.

Molecular mixing in a VD fluid. Density fields are initialized with symmetric bi-modal double delta PDFs with equal amounts of the two pure fluids. At low Atwood number, as might correspond to the Boussinesq case, the density PDF remains symmetrical as

the stirring and mixing proceeds. At high Atwood numbers, the PDF rapidly becomes skewed before decaying to uni-modal Gaussian-like distribution. The generation of skewness is due to the $\langle \rho(\rho,_j)^2 \rangle$ covariance which is close to zero for symmetric Gaussian-like density PDFs and for mixing in the Boussinesq case. Physically, this means that the heavy fluid undergoes less stirring and (consequently) less molecular mixing than the light fluid.

That this might be the case is suggested by the expression for the mean molecular mix rate

$$\varepsilon_{\rho v} = \mathscr{D} \left\langle \frac{\rho,_k}{\rho^{*3/2}} \frac{\rho,_k}{\rho^{*3/2}} \right\rangle , \qquad (6.1)$$

which implies that larger ρ^* events are accompanied by less mixing (for a given $\rho,_k$).

Because of the rapidity of the mixing of the light fluid, heavy pure fluid events are more frequent than light pure fluid events. This indicates that, though the PDF skewness generation mechanism $\langle \rho(\rho,_j)^2 \rangle$ is weighted to large-density events (by number and size), stirring, $\rho,_i u_{i,j} \rho,_j$, associated with the generation of $(\rho,_j)^2$ is much smaller in the large-density regions. It is conjectured that the inertia of the heavy fluid reduces the rate at which it is broken up by stirring, leading to smaller $(\rho,_j)^2$. Thus, heavy pure fluid blobs stay pure longer than the light fluid blobs.

Consequences for RT. For mixing in the high-Atwood-number RT layer, about which very little is known, this suggests that very different amounts of molecular mixing occur on different sides of the layer, leading to a longer penetration distance for the pure heavy fluid than the pure light fluid. This is probably the cause of the higher growth rates of the spikes versus the bubbles that was observed experimentally at high A by Dimonte & Schneider (2000). The bubble–spike anomaly is related to the production of the density skewness and the rate of molecular mixing

$$\frac{\mathrm{d}}{\mathrm{d}t} S = -S \frac{\varepsilon_\rho}{\langle \rho^2 \rangle} - \frac{3}{4} \frac{\langle \rho(\rho,_j)^2 \rangle}{\langle \rho,_k \rho,_k \rangle \langle \rho^2 \rangle^{1/2}} , \qquad \varepsilon_{\rho v} = \mathscr{D} \left\langle \frac{\rho,_k}{\rho^{*3/2}} \frac{\rho,_k}{\rho^{*3/2}} \right\rangle . \qquad (6.2)$$

This asymmetry is also seen in the medium Atwood simulations of Cabot & Cook (2006) as discussed in Livescu *et al.* (2008).

Mix metrics. The density PDFs show, as expected, that there is no correlation between lower-moment metrics and a unique mix state. This was made clear by comparing the density PDF for different cases when, as is characteristic of some laboratory RT measurements, $\theta = 0.65$. The PDFs for the cases when $\%_m = \theta = \Xi = \theta_{\langle \rho v \rangle} = 0.8$ also made this point clear. The PDFs obtained for the different cases at times $\%_m = \theta = \Xi = \theta_{\langle \rho v \rangle} = 0.8$ can have any shape; they can have either or neither pure fluids. In addition, the density PDF depends on all the parameters considered, A, Re_0, Fr and Sc. In contradistinction, the lower-order moments, θ and Ξ, appear to depend only on Re_{b_0} and Sc. Thus, the lower-order-moment evolutions in the VD case can be recovered from corresponding low A simulations (e.g. with Fr appropriately changed). Nevertheless, higher-order moments and the shape of the density PDF qualitatively change as the Boussinesq approximation is no longer valid.

Therefore, comparing integral quantities of the PDFs (low-order moments) between the VD and Boussinesq cases could lead to the false conclusion that there is no substantial difference in the mix states. As demonstrated, such moments cannot indicate anything about the presence or absence of pure fluid which corresponds

to events near tails of the PDF. Such events are not rare in the mixing of initially segregated pure fluids in which the PDFs are patently not quasi-Gaussian.

Relations between mix metrics. The commonly used θ mix parameter is related to the variance of the excess reactant:

$$\theta = 1 - \frac{\langle \rho^2 \rangle}{\langle \rho^2 \rangle_{nm}} = 1 - \frac{\langle \rho^2 \rangle}{(\bar{\rho} - \rho_1)(\rho_2 - \bar{\rho})}, \tag{6.3}$$

$$\theta = \left(1 - \langle X_e^2 \rangle\right)\left(1 + \frac{\tilde{\rho}^2}{\langle \rho^2 \rangle_{nm}}\right) = \varXi \frac{2 - \langle X_P^2 \rangle / \langle X_P \rangle}{2 - X_{P_{max}}}, \tag{6.4}$$

where $\tilde{\rho} = (\rho_1 + \rho_2)/2 - \bar{\rho}$. For the homogeneous case and in the central regions of the RT layer,

$$\theta|_H = 1 - \langle X_e^2 \rangle \tag{6.5}$$

and $\theta \geqslant \varXi$ (with $\varXi = \langle X_P \rangle$). Rigorous analytical bounds have been derived relating these quantities. For example, if $\varXi = 0.8$, then $0.8 \leqslant \theta \leqslant 0.96$.

Consequences for RT. From the expression above relating θ and $\varXi$, some comments for the RT layer were made. Near the centreline of an RT layer, the relations derived for the homogeneous case hold, and θ always over-predicts the mixing with respect to that predicted by $\varXi$. At the edges of an RT layer, θ always underpredicts the amount of mixing with respect to $\varXi$.

A VD mix metric. Owing to the appearance of $\langle \rho v \rangle$ in the moment equations for VD turbulence (and the absence of $\langle \rho^2 \rangle$), a new VD mix measure

$$\theta_{\rho v} = 1 - \langle \rho v \rangle / \langle \rho v \rangle_{nm}, \qquad \langle \rho v \rangle_{nm} = -\frac{(\rho_2 - \bar{\rho})(\bar{\rho} - \rho_1)}{\rho_1 \rho_2}, \tag{6.6}$$

is proposed.

The transport equation for the density PDF is formally the same as for the Boussinesq case and the dilatational effects do not appear explicitly. However, the dilatation sets the right-hand side of the $\langle \rho v \rangle$ equation which directly affects the mixing and the energy conversion mechanism. Conversely, for the Boussinesq case, the density variance mediates the energy conversion mechanism and the density variance equation is formally the same for the VD fluid. This again emphasizes the difference between mixing in a Boussinesq fluid as compared to a VD fluid.

Bounds on pure and mixed fluid quantities. Using only two lower-order moments, $(\theta, \bar{\rho})$ or $(\langle X_P \rangle, \bar{\rho})$, or $(\theta_{\rho v}, \bar{\rho})$, bounds on the composition of a general VD fluid were established. These bounds are valid for the RT layer as well. For example, if $\bar{\rho} = (\rho_1 + \rho_2)/2$, then for $\langle X_P \rangle = 0.8$, $0 \leqslant \%_B \leqslant 0.11$, $0.78 \leqslant \%_m \leqslant 1$; for $\theta = 0.8$, it yields $0 \leqslant \%_B \leqslant 0.2$, $0.75 \leqslant \%_m \leqslant 1$; and for $\theta_{\rho v} = 0.8$ and $A = 0.5$, it yields $0 \leqslant \%_B \leqslant 0.28$, $0.7 \leqslant \%_m \leqslant 1$. Any values in such intervals are possible. The tightest bounds are obtained when $(\bar{\rho}, \langle X_P \rangle)$ are known. These bounds can be used as realizability constraints and also to characterize the mixing state in low-dimensional models, in which low-order moments are typically the only information available. Nevertheless, first- and second-order moments cannot capture the skewness or the tails of the underlying density PDF, and bounds derived from only two such moments are formally the same for the pure light and pure heavy fluids.

Consequences for RT. In the RT layer, limitations evaluating the molecular mixing based on lower-moment metrics such as θ are clear: at the top of the layer the PDF is spiked at the black end and includes some grey. In the centre of the layer- the

PDF is quasi-Gaussian and the fluid grey. At the bottom of the layer, the PDF is spiked in the white with some grey. Yet across the layer, θ varies slowly, not giving an indication of the radically different amounts of white, black or grey. See Linden *et al.* (1994), Youngs (1994) and Wilson & Andrews (2001) for examples of such PDFs given by coarse-grained simulations.

Reynolds-number dependence. The evolution of mix variables changes little if the static Reynolds number increases above some critical value that depends on the Schmidt number. It is also observed that the higher the initial Re_{b_0}, the larger the maximum k, Re_t reached and, counter-intuitively, the less molecular mixing that takes place (for a given Sc).

Rate of molecular mixing. The density derivative PDF becomes asymmetric in the vertical direction, with wide tails, indicating that there are rare events corresponding to very large density-gradient magnitude. The frequency and size of these events, which correspond to fluid blobs moving towards each other, become larger with Sc and Re_{b_0} and significantly increase the resolution requirements.

Interfacial area scaling. For the cases considered, it is found that the interfacial surface area per unit volume of the $\rho^* = (\rho_1 + \rho_2)/2$ iso-density scales with the inverse of the density Taylor microscale: $\Sigma_{st} \propto \lambda_\rho^{-1}$.

Turbulence modelling. The eddy turnover time scales of $\langle \rho^2 \rangle$ and $\langle \rho v \rangle$ are not constant during the evolution of the flow, showing that the usual simple models for scalar dissipation are not useful for this flow. Furthermore, at higher Atwood numbers, the two time scales are different; this is probably due to the suggested lack of a one to one relation between $\langle \rho^2 \rangle$ and $\langle \rho v \rangle$ when there is a significant density difference present. Recall that the mixing mechanisms for $\langle \rho^2 \rangle$ and $\langle \rho v \rangle$,

$$\varepsilon_\rho = \mathscr{D} \langle \rho_{,k}\, \rho_{,j} \rangle, \qquad \varepsilon_{\rho v} = \mathscr{D} \left\langle \frac{\rho_{,k}}{\rho^{*3/2}} \frac{\rho_{,k}}{\rho^{*3/2}} \right\rangle,$$

are different only when there are large density differences: i.e. $\rho_{rms}/\bar{\rho} \sim 1$.

Schmidt-number-dependence of the integral length-scale ratio. The ratio of the integral length scales of the velocity and density fields is observed to be very sensitive to Schmidt number. For simulations with $Sc = 1$, the two integral scales are commensurate. For the $Sc \neq 1$, cases, they are surprisingly different. Given that the integral length scale is a large-scale quantity and that the only difference is the molecular diffusion coefficient, why this occurs is a mystery. The conundrum is compounded by the Taylor microscale ratio which, being a smaller-scale quantity, shows much less sensitivity to the Schmidt number.

Comment on the spectral energy balance. Inspection of the spectral energy equation indicates that in the viscous range, during the growth stage, the nonlinear transfer terms and the viscous terms are the same magnitude and, since they are of opposite sign, the anisotropic buoyancy production retains its relative importance even though it has small magnitude. Thus, during the growth stage, the normal stresses are anisotropic at the smallest scales, with some 50% of the energy in the vertical direction. The dissipation itself becomes more isotropic, substantiating the explanation above. The relative magnitude of the terms in the spectral kinetic energy equation was discussed by deriving expressions for critical wavenumbers which express the balance of various terms and time scales for cascade processes. Also observed was the isotropization of the intermediate scales as the nonlinear spectral transfer dominates

buoyancy production. The persistent viscous range anisotropy may have substantial relevance for LES type closures.

7. Conclusions

Surprising and substantial differences between the mixing processes in a VD flow, as opposed to the Boussinesq approximation, are found. It is observed that the pure heavy fluid mixes more slowly than pure light fluid and, as a consequence, an initially symmetric bi-modal double delta density PDF is rapidly skewed as the light pure fluid rapidly vanishes and only at long times does it relax to a symmetric Gaussian-like PDF. In the Boussinesq case, the density PDF is symmetrical throughout the mixing process as the light and heavy fluids mix at the same rate. For the VD RT configuration this suggests that molecular mixing proceeds differently on the two sides of the RT layer. Experiments to date have not investigated this possibility. In fact, it appears that there is only one laboratory RT experiment, Wilson & Andrews (2001), that measures the density PDF at different vertical locations.

The current simulations were motivated by several interests: (i) the need to understand if material mixing in a VD flow is phenomenologically different from that for the Boussinesq case and if this difference is important; (ii) to examine the changes in the turbulence structure as it couples with the material mixing in a buoyantly driven flow; and (iii) to provide a data set for the quantities, many of which are difficult to obtain experimentally, required by various type of closure. The results presented are, by and large, general and apply to a wide class of VD flows; they have also been verified with the in-homogeneous 3072^3 VD RT simulation of Cabot & Cook (2006) as shown in Livescu *et al.* (2008).

Diverse mixing metrics, describing both the state of the mix and their relation to the density PDF are studied. There is no fundamental or unique connection between such low-order metrics and the underlying physical mix state as is made clear by the very different forms of the PDF and the amount of pure and mixed fluids present. Nevertheless, these metrics may be the only ones available in low-dimensional models. Therefore, analytical bounds were derived to ascertain the range of fluid compositions that such metrics imply. The bounds can be used as realizability constraints in low-dimensional models or to characterize the flow configuration.

The traditional RT mix parameter, θ, is shown to be related to the variance of the unmixed fluid (the excess reactant in a hypothetical fast reaction) and not connected to the amount of mixed fluid. Analytical bounds between θ and $\varXi$ have also been derived. A new mix measure, based on $\langle\rho v\rangle$ and related to the mean specific volume, appropriate for VD turbulence and appearing in the Favre-averaged second-moment equations, was proposed. Bounds on fluid composition given only $\langle\rho v\rangle$ and $\bar{\rho}$ were derived.

The rate at which mixing occurs depends on both the magnitude of the density gradients and the interfacial surface area. The PDF of the vertical derivative of the density is asymmetric at higher A, as in the 'heavy over light fluid' configuration, the magnitude of the density gradients increases considerably. This affects the shape of the fluid blobs and substantially increases the resolution requirements at high Atwood numbers. The stoichiometric density surface area was found to scale with density Taylor microscale for the Schmidt numbers considered in this study ($Sc = 0.1, 0.5, 1, 2$).

The large scales of the flow remain anisotropic at all times owing to the buoyancy production. It is shown that buoyancy production is small compared to nonlinear and viscous effects in the spectral energy equation at high wavenumbers, so that the

intermediate scales, in a high-Reynolds-number flow, become isotropic shortly after the sudden application of the buoyancy force. However, if Sc is not very small, there is a persistent anisotropy of the smallest scales during the growth stage, as in the viscous range there is a cancellation between the viscous and nonlinear effects and buoyancy production remains important.

To summarize: (i) mixing in a Boussinesq flow is not a relevant model for mixing in a VD flow except when the density PDF is of the uni-modal Gaussian type, the density fluctuations small, and no pure fluid is present; (ii) mixing in the Boussinesq case becomes a useful model if all that is required is low-order integral measures of the density PDF and no measures of the fluid composition; (iii) given two low-order moments of the density PDF it is possible to establish useful bounds on the fluid composition; (iv) in a VD flow mixing becomes asymmetric, with the pure light fluid disappearing faster than the pure heavy fluid; and (v) buoyancy production changes the turbulence structure with persistent anisotropy of the smallest scales.

REFERENCES

BATCHELOR, G. K., CANUTO, V. M. & CHASNOV, J. R. 1992 Homogeneous buoyancy-generated turbulence. *J. Fluid Mech.* **235**, 349–378.

BESNARD, D., HARLOW, F. H., RAUENZAHN, R. M. & ZEMACH, C. 1992 Turbulence transport equations for variable-density turbulence and their relationships to two field models. *Tech. Rep.* Los Alamos National Laboratory, lA-12303-MS.

CABOT, W. H. & COOK, A. W. 2006 Reynolds number effects on Rayleigh–Taylor instability with possible implications for type-ia supernovae. *Nature Phys.* **2**, 562–568.

COOK, A. W. & DIMOTAKIS, P. E. 2001 Transition stages of Rayleigh–Taylor instability between miscible fluids. *J. Fluid Mech.* **443**, 69–99.

COOK, A. W. & ZHOU, Y. 2002 Energy transfer in Rayleigh–Taylor instability. *Phys. Rev.* E **66**, 026312–1–026312–12.

DALZIEL, S. B., LINDEN, P. F. & YOUNGS, D. L. 1999 Self-similarity and internal structure of turbulence induced by Rayleigh–Taylor instability. *J. Fluid Mech.* **399**, 1–48.

DIMONTE, G. & SCHNEIDER, M. 2000 Density ratio dependence of Rayleigh–Taylor mixing for sustained and impulsive acceleration histories. *Phys. Fluids* **12**, 304–321.

GEORGE, E. & GLIMM, J. 2005 Self-similarity of Rayleigh–Taylor mixing rates. *Phys. Fluids* **17**, 054101–1–13.

GIVI, P. 1989 Model-free simulations of turbulent reacting flows. *Prog. Energy Combust. Sci.* **15**, 1–107.

KRAICHNAN, R. H. 1971 Inertial-range transfer in two- and three-dimensional turbulence. *J. Fluid Mech.* **47**, 525–535.

LINDEN, P. F., REDONDO, J. M. & YOUNGS, D. L. 1994 Molecular mixing in Rayleigh–Taylor instability. *J. Fluid Mech.* **265**, 97–124.

LIU, X., GEORGE, E., BO, W. & GLIMM, J. 2006 Turbulent mixing with physical mass diffusion. *Phys. Rev.* E **73**, 016304–1–5.

LIVESCU, D. & RISTORCELLI, J. R. 2007 Buoyancy-driven variable-density turbulence. *J. Fluid Mech.* **591**, 43–71.

LIVESCU, D., JABERI, F. A. & MADNIA, C. K. 2000 Passive scalar wake behind a line source in grid turbulence. *J. Fluid Mech.* **416**, 117–149.

LIVESCU, D., JABERI, F. A. & MADNIA, C. K. 2002 The effects of heat release on the energy exchange in reacting turbulent shear flow. *J. Fluid Mech.* **450**, 35–66.

LIVESCU, D., RISTORCELLI, J. R., GORE, R. A., DEAN, S. H., CABOT, W. H. & COOK, A. W. 2008 High Reynolds number Rayleigh–Taylor turbulence. *J. Turbul.* (submitted).

Muenshke, N. J., Andrews, M. J. & Schilling, O. 2006 Experimental characterization of spatio-temporal evolution of small Atwood number Rayleigh–Taylor mixing layer. *J. Fluid Mech.* **567**, 27–61.

Pope, S. B. 1985 PDF methods for turbulent reacting flows. *Prog. Energy Combust. Sci.* **11**, 119–192.

Pope, S. B. 1988 Evolution of surfaces in turbulence. *Intl. J. Engng. Sci.* **26**, 445–469.

Ramaprabhu, P. & Andrews, M. J. 2004 Experimental investigation of Rayleigh–Taylor mixing at small Atwood numbers. *J. Fluid Mech.* **502**, 233–271.

Ristorcelli, J. R. 2006 Passive scalar mixing: analytical study of time scale ratio, variance and mix rate. *Phys. Fluids* **18**, 075101–1–075101–17.

Ristorcelli, J. R. & Clark, T. T. 2004 Rayleigh–Taylor turbulence: self-similar analysis and direct numerical simulations. *J. Fluid Mech.* **507**, 213–253.

Sandoval, D. L. 1995 The dynamics of variable density turbulence. PhD thesis, University of Washington, LANL Rep. LA-13037-T.

Sandoval, D. L., Clark, T. T. & Riley, J. J. 1996 Buoyancy-generated variable density turbulence. In *Proc. IUTAM Symp. on Variable Density Low Speed Turbulent Flows*, pp. 847–864. Kluwer.

Vervisch, L., Bidaux, E., Bray, K. N. C. & Kollman, W. 1995 Surface density function in premixed turbulent combustion modeling, similarities between probability density function and flame surface approaches. *Phys. Fluids* **7**, 2496–2503.

Warhaft, Z. & Lumley, J. L. 1978 An experimental study of the decay of temperature fluctuations in grid-generated turbulence. *J. Fluid Mech.* **88**, 659–684.

Williams, F. A. 1985 *Combustion Theory*. Perseus Cambridge.

Wilson, P. N. & Andrews, M. J. 2001 Spectral measurements of Rayleigh–Taylor mixing at low Atwood number. *Phys. Fluids* **14**, 938–945.

Young, Y. N., Tufo, H., Dubey, A. & Rosner, R. 1999 On the miscible Rayleigh–Taylor instability: two and three dimensions. *J. Fluid Mech.* **447**, 377–408.

Youngs, D. L. 1991 Three-dimensional numerical simulation of turbulent mixing by Rayleigh–Taylor instability. *Phys. Fluids* A **3**, 1312–1320.

Youngs, D. L. 1994 Numerical simulation of mixing in Rayleigh–Taylor and Richtmeyer–Meshkov instabilities. *Laser Part. Beams* **12**, 725–750.